

Nuclear Transparency in $90^\circ_{c.m.}$ Quasielastic A(p,2p) Reactions

J. Aclander^{7,†}, J. Alster^{7,†}, G. Asryan^{1,b,†}, Y. Averiche^{5,†}, D. S. Barton^{1,‡}, V. Baturin^{2,a,†}, N. Bukhtoyarova^{1,a,†}, G. Bunce^{1,‡}, A. S. Carroll^{1,c,‡}, N. Christensen^{3,d,†}, H. Courant^{3,‡}, S. Durrant^{2,†}, G. Fang^{3,§}, K. Gabriel^{2,†}, S. Gushue^{1,‡}, K. J. Heller^{3,§}, S. Heppelmann^{2,†}, I. Kosonovsky^{7,†}, A. Leksanov^{2,†}, Y. I. Makdisi^{1,‡}, A. Malki^{7,†}, I. Mardor^{7,†}, Y. Mardor^{7,†}, M. L. Marshak^{3,‡}, D. Martel^{4,†}, E. Minina^{2,†}, E. Minor^{2,†}, I. Navon^{7,†}, H. Nicholson^{8,†}, A. Ogawa^{2,†}, Y. Panebratsev^{5,†}, E. Piassetzky^{7,†}, T. Roser^{1,†}, J. J. Russell^{4,‡}, A. Schetkovsky^{2,a,†}, S. Shimanskiy^{5,†}, M. A. Shupe^{3,e,§}, S. Sutton^{8,†}, M. Tanaka^{1,f,†}, A. Tang^{6,†}, I. Tsetkov^{5,†}, J. Watson^{6,†}, C. White^{3,†}, J.-Y. Wu^{2,†}, D. Zhalov^{2,†}

¹ Brookhaven National Laboratory, Upton, NY 11973-5000, USA

² Pennsylvania State University, University Park, Pennsylvania 16802, USA

³ University of Minnesota, Minneapolis, Minnesota 55455, USA

⁴ University of Massachusetts Dartmouth, North Dartmouth, Massachusetts 02747, USA

⁵ J.I.N.R., Dubna, Moscow 141980, Russia

⁶ Dept. of Physics, Kent State University, Kent, Ohio 44242, USA

⁷ School of Physics and Astronomy, Tel Aviv University, Tel Aviv 69978, Israel

⁸ Dept. of Physics, Mount Holyoke College, South Hadley, Massachusetts 01075, USA

^a Home Institution is Petersburg Nuclear Physics Institute, Gatchina, St Petersburg 188350, Russia

^b Home Institution is Yerevan Physics Institute, Yerevan 375036, Armenia

^c Now at 71 Kendal Drive, Oberlin, Ohio 44074, USA

^d Now at Carleton College, Northfield, Minnesota 55057, USA

^e Now at University of Arizona, Tucson Arizona 85721, USA

^f deceased

[§] Member of AGS Experiment 834.

[†] Member of AGS Experiment 850.

[‡] Member of AGS Experiments 834 and 850.

(Dated: May 24, 2004)

We summarize the results of two experimental programs at the Alternating Gradient Synchrotron of BNL to measure the nuclear transparency of nuclei measured in the A(p,2p) quasielastic scattering process near 90° in the pp center of mass. The incident momenta varied from 5.9 to 14.4 GeV/c, corresponding to $4.8 < Q^2 < 12.7(\text{GeV}/c)^2$. Taking into account the motion of the target proton in the nucleus, the effective incident momenta extended from 5.0 to 15.8 GeV/c. First, we describe the measurements with the newer experiment, E850, which had more complete kinematic definition of quasielastic events. E850 covered a larger range of incident momenta, and thus provided more information regarding the nature of the energy dependence of the nuclear transparency. In E850 the angular dependence of the nuclear transparency near 90° , and the nuclear transparency for deuterons was studied. Second, we review the techniques used in an earlier experiment, E834, and show that the two experiments are consistent for the Carbon data. E834 also determines the nuclear transparencies for lithium, aluminum, copper, and lead nuclei as well as for Carbon. A determination of the (π^+, π^+p) transparencies is also reported. We find for both E850 and E834 that the A(p,2p) nuclear transparency, unlike that for A(e,e'p) nuclear transparency, is incompatible with a constant value versus energy as predicted by Glauber calculations. The A(p,2p) nuclear transparency for Carbon and Aluminum increases by a factor of two between 5.9 and 9.5 GeV/c incident proton momentum. At its peak the A(p,2p) nuclear transparency is $\sim 80\%$ of the constant A(e,e'p) nuclear transparency. Then the nuclear transparency falls back to a value at least as small as that at 5.9 GeV/c, and is compatible with the Glauber level again. This oscillating behavior is generally interpreted as an interplay between two components of the pN scattering amplitude; one short ranged and perturbative, and the other long ranged and strongly absorbed in the nuclear medium. A study of the A dependent nuclear transparency indicates that the effective cross section varies with incident momentum and is considerably smaller than the free pN cross section. We suggest a number of experiments for further studies of nuclear transparency effects.

PACS numbers: 13.85.Dz

I. INTRODUCTION

If the nucleons in a nucleus were at rest and very lightly bound, then nuclear transparency for A(p,2p) reactions as illustrated in Figure 1 would simply be the ratio of the

differential cross section for quasielastic scattering from the protons in the nucleus (e.g. Carbon), to the differential cross section for free pp scattering corrected for the number of protons in the nucleus, Z. The nuclear transparency is then a measure of the survival probability for

the protons to enter and exit the nucleus without interacting with the spectator nucleons in the target nucleus. The actual situation is significantly complicated by the momentum and binding energy distributions described by the spectral function of the protons in the nucleus. Note that in this paper we will be implicitly integrating the spectral functions over the binding energy distributions and considering only the nuclear momentum distributions. Even with the assumption that the scattering can be factorized, a detailed knowledge of the behavior of the elementary pp differential cross section, and of the spectral function of the nucleus is required since the pp differential cross section at large angles depends so strongly on energy. In the experiments described below, either a sample of protons with a narrow range longitudinal momentum is selected, or the observed quasielastic distributions are corrected with the known differential pp cross section. Similar transparencies can be defined for other quasielastic scattering processes by other incident hadrons or leptons. Transparencies for $A(e,e'p)$ have been extensively measured as discussed below.

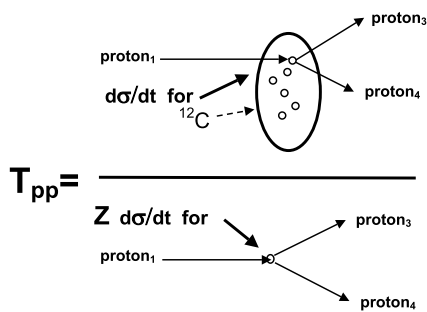


FIG. 1: Illustration of the quantities used in the determination of nuclear transparency for a representative nucleus, ^{12}C in the numerator, for free pp scattering in the denominator. The incident proton is $proton_1$, and the struck proton is $proton_2$. The two outgoing protons are designated as $proton_3$ and $proton_4$.

In this paper we report on the combined results of two AGS experiments to measure the nuclear transparency of nuclei in the $A(p,2p)$ quasielastic scattering process near 90° in the pp center of mass (c.m.). In the first part of the paper we describe the measurements with the newer experiment, E850, which features a more complete kinematic definition of the quasielastic events. E850 extends the range of incident energies, and provides more information regarding the nature of the unexpected fall in the nuclear transparency above $9.5 \text{ GeV}/c$ [1],[2]. In the second part, we review the techniques used in the earlier E834 experiment [3]. For the E834 experiment, the directions of each final state particle were determined but the momentum of only one track was measured. The E850 experiment allows full and symmetrical tracking with momentum reconstruction of both final state particles.

The E850 measurement addresses the concerns about the background subtraction in the determination of the quasielastic signal in the E834 experiment. We show for the overlapping Carbon measurements that these two experiments are consistent in the energy dependence of the nuclear transparency. E834 measures the nuclear transparency for five different nuclei, and also yields initial results regarding transparencies for $A(\pi^+, \pi^+p)$ interactions [4]. While most of the principal results have been reported previously, we present a more detailed and consistent view of the two programs.

Other measurements with these two detectors allow us to investigate a number of the factors involved with the measurement and interpretation of nuclear transparency. The publication of Y. Mardor, *et al.* reported on a study of the factorization assumption, and the equality of the longitudinal and transverse portions of the nuclear momentum distribution for the Carbon nucleus [5]. Short range correlations, which give rise to the high momentum tails of the momentum distributions were reported in papers by Aclander, *et al.*, Tang, *et al.*, and Malki, *et al.* [6, 7, 8]. $A(p,2p)$ measurements from both the E834 detector by Heppelmann, *et al.* [9], and the E850 detector by Y. Mardor, *et al.* [5] showed that the nuclear momentum distributions determined in $A(p,2p)$ reactions were in agreement with those found by $A(e,e'p)$ experiments.

Color transparency refers to a QCD phenomenon, independently predicted in 1982 by Brodsky [10] and Mueller [11], involving a reduction of soft interactions, in both the initial (ISI) and final (FSI) states, for a hard quasielastic scattering. These theorists deduced from QCD that when a proton traversing the nucleus experiences a hard collision, a special quantum state is selected. That special state involves the part of the proton wave function that is most ‘shock resistant’ and tends to survive the hard collision without breaking up or radiating gluons. This state is also expected to survive long enough while traveling through the nucleus to have a reduced interaction with the spectators in the target nucleus. The state is predicted to involve a rare component of the proton wave function that is dominated by 3 valence quarks at small transverse spatial separation. The color transparency prediction of QCD is that the fraction of nuclear protons contributing to $A(p,2p)$ quasielastic scattering should increase from a nominal level consistent with Glauber absorption [12, 13], at low Q^2 , and then to approach unity at very high Q^2 . However, the fall of nuclear transparency above $9.5 \text{ GeV}/c$ indicates that additional amplitudes are required.

Due to the very steep dependence of the 90° pp cross section on the center of mass energy squared, s^{-10} , and the uncertainties in the nuclear momentum distributions, it is useful to measure a ratio close to the kinematic point where the target proton is at rest, particularly in the longitudinal direction. This ratio will demonstrate the energy dependence of the nuclear transparency with a minimum of assumptions. We refer to this as the nuclear transparency ratio, T_{CH} , for quasielastic scattering on

Carbon, compared to that for hydrogen. Then using our best knowledge of the energy dependence of the pp cross section, and the nuclear momentum distributions we can determine the nuclear transparency, T_{pp} , integrated in the entire longitudinal direction.

There have been a number of investigations of nuclear transparency in addition to those involving quasielastic reactions. Transparencies in exclusive incoherent ρ^0 production have been measured at Fermilab, CERN, and DESY. At Fermilab [14], increases in exclusive nuclear transparency have been measured as the photon becomes more virtual, as expected in the color transparency picture. CERN data, also involving muon production of ρ^0 's, but at higher Q^2 , indicate that the effect is smaller [15]. Coherence length effects have been investigated in the HERMES experiment at DESY [16]. It is important to distinguish between coherence length, which is the distance at which the virtual photon fluctuates into a $q\bar{q}$ pair, and the formation length in which the initially point like $q\bar{q}$ pair grows to the normal ρ^0 size. It is the formation length that enters into the determination of color transparency. The coherence length is not a factor in quasielastic scattering.

Another important investigation of nuclear transparency has been the coherent diffractive dissociation of 500 GeV/c π^- into di-jets on nuclear targets at $Q^2 > 7(GeV/c)^2$ [17]. Unlike the other experiments, di-jet production is not an exclusive reaction, and therefore its interpretation may be different than other searches for color transparency. The power law behavior with A determined from the A -dependence in this experiment is considerably larger, ~ 1.5 than the ~ 0.7 usually found in inclusive πA reactions. The very high energy of this experiment makes color transparency effects likely, but does not allow a study of the threshold for nuclear transparency.

This paper will confine itself to only quasielastic reactions, which have involved incident hadrons, p and π^+ , and those with incident electrons. The mechanisms of these quasielastic reactions are closely related, and therefore can be compared in a relatively straightforward manner.

II. EXPERIMENT E850

This section will cover measurements of nuclear transparency with the E850 detector during two experimental runs. Details of the detector characteristics, and of the kinematical analysis are discussed.

A. The E850 Detector (EVA)

A 24 GeV proton beam from the AGS produced secondary hadrons at 0° through its interaction with a ~ 3 cm long platinum target. After magnets in the C1 transport line dispersed the secondary hadrons with respect to

charge and momentum, collimators selected the particles to be transported to the experiment. The momentum spread of the beam was typically $\pm 0.5\%$. Every 3 seconds, up to 5×10^7 particles in a 1 second long spill were delivered to a 1×2 cm^2 spot. Two, pressurized CO_2 , differential Čerenkov counters, ~ 30 m upstream of the detector, allowed identification of the pions, kaons and protons in the incident beam on a particle-by-particle basis [18, 19]. The incident particles were tracked by a series of scintillation hodoscopes along the beam line. We measured the incident beam flux with an ion chamber cross-calibrated with direct particle counting at lower intensities, and then corrected for the proton fraction with the differential Čerenkov counters. The final hodoscope was the one denoted by BH just before the nuclear targets in Figure 2.

The E850 experiment embedded the Carbon (C), CH_2 , and CD_2 targets inside a 2 m diameter, 3 m long superconducting solenoid with a 0.8 T field as shown in Figure 2. The solenoid was a modification the CLEO I solenoid originally used at Cornell [20]. The pole piece intercepts most of the magnetic flux emerging from the solenoid to form a reasonably uniform, horizontal magnetic field through out the solenoid volume. The precise shape of the field was determined by a combination of a large number of Hall probe measurements in regions of high gradients and 3-D mesh calculations [21]. The annular space between the pole piece and the solenoid allowed particles scattered near $90^\circ_{c.m.}$ to reach the detectors outside the solenoid. This arrangement facilitates easier triggering and better momentum resolution than having all the detector elements inside the solenoid. The targets were 5.1×5.1 cm^2 in area, and 6.6 cm in length, spaced ~ 20 cm apart. The positions of the C, CH_2 and CD_2 targets were interchanged regularly to minimize the differences in flux and acceptance.

Surrounding the targets were four concentric cylinders (C1-C4) of mean radii: 10, 45, 90, and 180 cm. Each cylinder was fabricated from four layers of thin wall straw tubes (114 μm Mylar with 8 μm of aluminum cladding except for C4, which had double the wall thickness). Their diameters were 0.50, 1.04, 1.04, and 2.16 cm, and their total number was 5632 [22]. C1 and C2 were complete cylinders, but C3 and C4 had small gaps ($\sim 2\%$ and $\sim 5\%$ in the azimuthal coverage) at the top and bottom to allow for support structures. They were filled with a 50-50 mixture of Argon-Ethane at slightly above atmospheric pressure. All the tubes measure the drift distance from the track to the central wire with an accuracy of 150 μm , and for C2-C4, the longitudinal distance was measured to $\sigma \simeq 2$ cm by charge division [23],[24]. The momentum resolution was dominated by multiple scattering, and was $\sigma(p)/p \simeq 7\%$ as determined from pp elastic scattering. The tracks scattered near 90° c.m. passed through the annulus between the solenoid and the steel pole piece until they reached the two fan-shaped scintillation counter arrays, H1 and H2, and the two larger straw tube cylinders, C3 and C4.

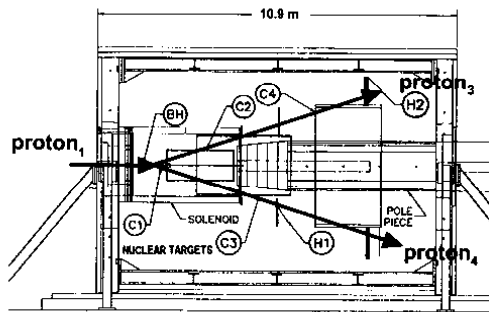


FIG. 2: Schematic Drawing of E850 solenoidal detector, which shows a vertical, midplane section. C1-C4 are the four-layer arrays of straw tube cylinders. C1 and C2 were completely within the solenoid, while C3 was only partially inside the solenoid. C, CH₂, and CD₂ targets were located inside the C1 straw tube cylinder. The counter-weighted pole piece returns the magnetic flux emerging from the right hand end of the solenoid. A re-entrant cavity in the pole piece absorbs the incident beam downstream of the detecting elements. H1 and H2 were the scintillation trigger counters of about 256 elements each. The bold arrows show typical trajectories of the incident particle, *proton*₁ and two scattered protons, *proton*₃ and *proton*₄. For scale, the length of the magnet frame was 10.9m, and the straw tube cylinders (C2, C3, and C4) were 2m long.

As illustrated in Figure 3 the trigger system selects only events with particles above a minimum transverse momentum, P_T [23]. This selection was done in two stages. The first selection was done in ~ 75 nsec by checking the correlation in ϕ between H1 and H2. Then a second more precise selection was performed by logic arrays, which measured the momentum by a 3-point correlation with the hits in the cylinders labeled C2, C3 and C4. The time that this calculation took was $\sim 1\mu\text{sec}$, but depended on the complexity of the event. Some further checks were carried out by microprocessors attached to this trigger system to insure that there were two tracks and they were very crudely coplanar. A microprocessor then read out the CAMAC based TDC's and the FAST-

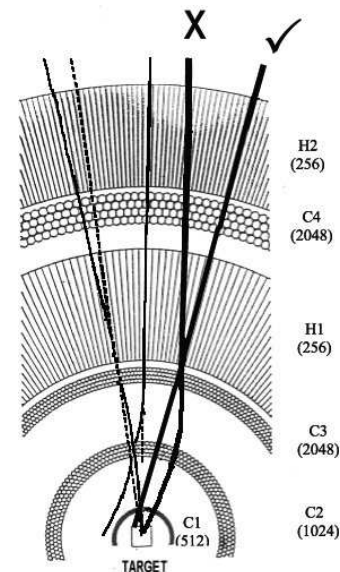


FIG. 3: A transverse (r - ϕ) projection of a portion of the spectrometer (EVA) used for E850. C1-C4 are cylinders of straw tubes, and H1 and H2 are hodoscope arrays of scintillation counters. The relative sizes of the elements are only approximate. Radially, the coil of the superconducting solenoid just surrounds the C3 cylinder, and the magnetic field is nearly confined within this radius. The number of elements listed for each array is nominal. A few elements are missing in top and bottom in C3, C4 and H2 to allow for support structures. C1, C2 and H1 cover the entire azimuth. The elements of H2 were one-third overlapped to provide twice the resolution in ϕ . The curved track labeled with the \times was rejected by the trigger system, while the higher momentum, straighter track indicated by the \checkmark was accepted.

BUS based ADC's from the straw tubes and scintillation counters. Details of these trigger systems can be found in the reference of Wu, et al [23]. Figure 4 shows the inclusive pp cross section at 90° for 8 GeV/c incident protons, and the approximate trigger efficiency, which rejects low p_T inelastic backgrounds while retaining all of the events near the exclusive limit. This arrangement provided an acceptable trigger rate of less than 100 Hz for incident beams of up to 10^8 Hz ($\sim 10^7$ interactions per spill).

In a large detector such as EVA, the location, identification, and measurement of tracks is a complex matter that will only be described briefly in this article. For more detailed information, see the theses of References [26],[27],[28],[29],and [30]. The initial location of all the straw tube elements was determined using a precision 3-D survey using the computer linked ManCat (surveying) system [31]. This achieved a precision of better than 1 mm, which was further reduced to $\sim 150\mu\text{m}$ by fitting to magnet-off, straight tracks.

Legitimate hits in the straw tubes were selected by checking that the drift times were within physical limits, and that the ADC values were above the noise level.

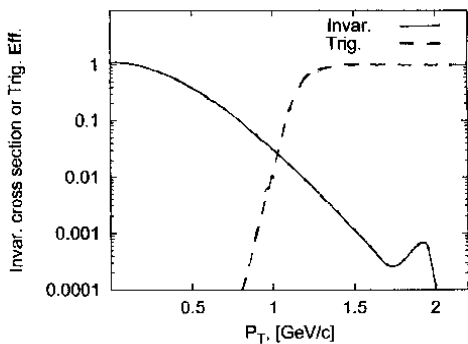


FIG. 4: The 8 GeV/c invariant cross section at $90_{c.m.}^{\circ}$ for $pp \rightarrow p + X$, normalized to 1 at $P_T = 0$, is shown as the solid line [25]. The peak at the end is a representation of elastic scattering contribution. An approximate E850 trigger acceptance is shown as the dashed line.

Neighboring hits within the 4 layers of each cylinder were collected into ‘bunches’ of typically 3 or 4 hits. Then these ‘bunches’ were combined with the ‘bunches’ from the other cylinders to form complete tracks. A multi-step process was used to select the best hits in the case of ambiguities, and find the best fit to the tracks’ curvature in the magnetic field. The sagitta of these tracks in the $r - \phi$ plane between C1 and C3, and the deviation from the straight line extended inward from hits in C3 and C4 were used to determine the particles’ momentum. Charge division as measured by the ADC values read from the two ends of the straw tubes determined the z-coordinates of the straws selected in the $r - \phi$ fit. These z coordinates in turn were fit to calculate the polar angles of the tracks. Final selections of events were the result of an adequate χ^2 to the $r - \phi$ fit, and a consistency of the vertex position as determined by the two tracks.

B. Kinematics for E850

In this experiment, the exclusive quasielastic process involves a single hard pp interaction with $Q^2 >$

$4(\text{GeV}/c)^2$. The final state consists of two energetic protons and a residual excited nucleus. The presence of more than two tracks in the detector identified the class of events with primary and secondary inelastic interactions. This allowed for background subtraction as described below.

The fundamental sub-process of our quasielastic events is the pp interaction

$$proton_1 + proton_2 \rightarrow proton_3 + proton_4$$

at a pp scattering angle near 90° c.m.. We associate $proton_1$ with the beam particle, and $proton_2$ with the target proton in the nucleus. The quasielastic events are characterized by a small missing energy, ϵ_m , and missing momentum, \vec{P}_m . We define missing energy, missing momentum and missing mass squared, m_M^2 , in terms of measured P_i , and resulting energy, E_i of each $proton_i$:

$$\begin{aligned} \epsilon_m &= E_3 + E_4 - E_1 - m_p \\ \vec{P}_m &= \vec{P}_3 + \vec{P}_4 - \vec{P}_1 \\ m_M^2 &= \epsilon_m^2 - \vec{P}_m^2. \end{aligned} \quad (1)$$

In the spirit of the impulse approximation we identify the measured missing momentum with the momentum of the struck proton inside the nucleus. For quasielastic scattering at c.m. scattering angles of 90° , the pair of final state protons is produced at approximately equal momenta, polar angles and opposite azimuth angles. The simple symmetrical nature of the final state is altered by three classes of phenomena: the small variation in c.m. scattering angles around 90° ; the effects of the motion of the struck proton determined by the nuclear momentum distribution and the interaction of initial or final state protons with the spectator nucleons in the nucleus.

By including a range of c.m. scattering angles around 90° , one induces a spread in the final state energies and polar angles, which are proportional to the $\cos(\theta_{c.m.})$ [1]. The detector is configured to have acceptance for c.m. scattering angles in the range $\sim 86^{\circ} < \theta_{c.m.} \leq 90^{\circ}$ at each beam energy as listed in Table I of the Appendix.

The removal of a proton with momentum, \vec{P}_m , from the nucleus implies a transfer of that three momentum from the nucleus to the observed two-proton final state. A small deficit in final state energy, ϵ_m , also can in principle be observed. We define the \hat{z} direction to coincide with the incident beam direction. The final state proton pair has transverse momentum, \vec{P}_{mT} with the \hat{x} direction to be in the scattering plane of $proton_3$ and \hat{y} to be normal to this scattering plane. By our convention, $proton_3$ has the smaller polar angle. So components of the nuclear momentum are:

$$\begin{aligned} \vec{P}_m &= (P_{mx}, P_{my}, P_{mz}) \\ \vec{P}_{mT} &\equiv P_{mx}\hat{x} + P_{my}\hat{y}. \end{aligned} \quad (2)$$

The in-plane momentum component, P_{mx} , depends directly on the the difference of the x-components of \vec{P}_3

and \vec{P}_4 . Hence, P_{mx} has broader resolution than the out-of-plane component, P_{my} , which is largely determined from the azimuthal angles. The distribution of the P_{mT} variables for the hydrogen events in CH_2 , is shown in Figure 5.

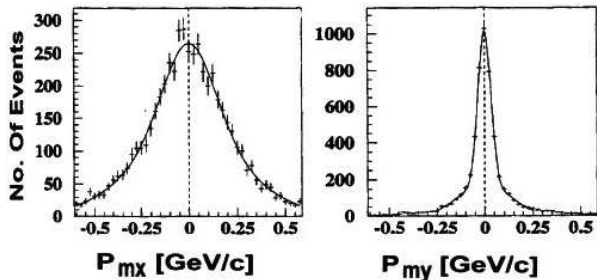


FIG. 5: The distribution of the transverse components of the missing momenta, P_{mx} and P_{my} , for selected hydrogen events from the CH_2 targets for 5.9 GeV/c. The width of the P_{mx} distribution is $\sigma = 0.150$ GeV/c and for the P_{my} distribution it is $\sigma = 0.035$ GeV/c.

To account for the effects of longitudinal component of the nuclear momentum it is useful to consider the momentum distribution in light cone coordinates. Defining $E_m = \epsilon_m + m_p$, the light cone momentum components are derived from the nuclear momenta: $(E_m, p_{mz}) \rightarrow (E_m \pm p_{mz})$. The ordinary nucleon momentum distribution can be re-expressed as a distribution function of light cone components. The ratio of the dimensionless light cone fraction carried by a single proton to that carried by the entire nucleus is α/A . Specifically, we write

$$\alpha \equiv A \frac{(E_m - P_{mz})}{M_A} \simeq 1 - \frac{P_{mz} - \epsilon_m}{m_p} \simeq 1 - \frac{P_{mz}}{m_p}. \quad (3)$$

The approximate expression for α comes from neglecting ϵ_m and taking the mass of the nucleus $M_A \simeq Am_p$.

Analogous to the use of pseudo-rapidity based on angles as an approximation to rapidity, which includes the particles' momentum, we define

$$\alpha_0 \equiv 1 - \frac{2\beta \cos \frac{\theta_3 - \theta_4}{2} \cos \frac{\theta_3 + \theta_4}{2} - p_{1z}}{m_p}$$

with

$$\beta \equiv \sqrt{\left(\frac{E_1 + m_p}{2}\right)^2 - m_p^2} \quad (4)$$

For a given beam momentum, α_0 is a function only of the final state lab polar angles, θ_3 and θ_4 , and not the final state momenta, P_3 and P_4 . It is obtained from the exact expression by assuming that the final state momenta, β , are equally shared between two final state protons. For the limited range of angles of this experiment, $\cos \frac{\theta_3 - \theta_4}{2}$ is ~ 1.0 . Since for our experiment α_0 is better determined than α , we use α_0 in our analysis. The distribution of α_0 for selected CH_2 events at 5.9 GeV/c is

shown in Figure 6. The resolution of the α_0 distribution is $\sigma = 0.025$, and calculations indicate the difference between α and α_0 is less than 0.005 for our range of angles..

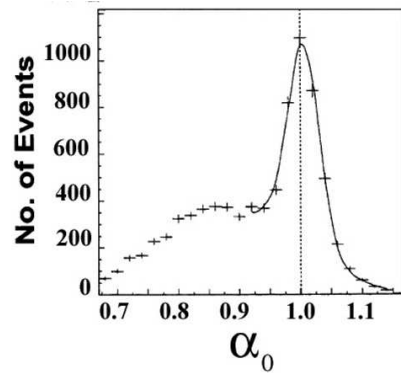


FIG. 6: The distribution of the longitudinal component of the light cone momentum, α , for selected hydrogen events from the CH_2 targets. The approximation, α_0 , is substituted for α as described by Equation 4.

The width (~ 200 MeV/c) of the nuclear momentum distribution for the longitudinal momentum results in approximately a 20% spread in the measured α distribution around unity. Because the measured distribution is strongly influenced by the s^{-10} behavior of the pp cross section, the shape of the distribution is strongly skewed toward $\alpha < 1$. In the kinematic region of interest, the center of mass energy of the $pp \rightarrow pp$ sub-process will be nearly independent of \vec{P}_{mT} but will depend critically upon α . For fixed beam energy, E_1 , we find that s (the square of the center of mass energy of the pp system) depends on α according to:

$$\begin{aligned} s &\simeq \alpha s_0 \\ s_0 &= 2m_p E_1 + 2m_p^2 \end{aligned} \quad (5)$$

where s_0 corresponds to the value of s for the case of the struck proton at rest ($\alpha = 1$). In this paper we will consider an effective incident beam momentum P_{eff} calculated from an effective beam energy, E_{eff} :

$$E_{eff} = \frac{s}{2m_p} - m_p \simeq E_1 \alpha \quad (6)$$

where the approximation reflects the relativistic limit. Use of the variable P_{eff} has been studied in References [5, 27].

We identify the missing momentum of Equation 1 with the momentum of the nucleon in the nucleus in the spirit of the impulse approximation. In the longitudinal direction this is a very good approximation. In the transverse direction, this relation is less exact because of elastic re-scattering. Because the $90^\circ_{c.m.}$ pp cross section strongly depends on one longitudinal light-cone component of the missing momentum, we express the missing momentum in light-cone coordinates. The coordinate system takes \hat{z} as the beam direction and \hat{y} normal to the scattering

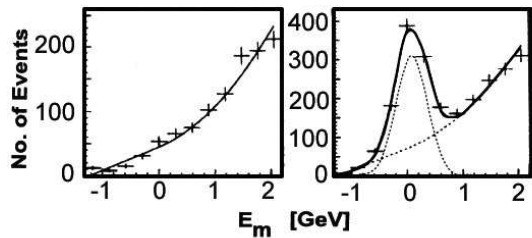


FIG. 7: Missing-energy, E_m , distribution for $P_1 = 5.9$ GeV/c. The left hand figure is plot shows the events with one or more extra tracks in the straw tubes. The right hand plot is the E_m distribution with no extra tracks. The dotted line represents the quasilastic distribution after the interpolated background is subtracted.

plane. In the first E850 publication regarding nuclear transparency, the separation of signal from background was done in the missing-energy (E_m) distribution as illustrated in Figure 7 [1]. A model for the background distribution, based on events with at least one extra track observed in the straw tube cylinders provided a parameterized shape for the background subtraction. Although this method was satisfactory for the 5.9 and 7.5 GeV/c analysis, it became less satisfactory as the incident momentum increases and the missing energy resolution broadens.

We now describe an improved analysis procedure used for the second publication where the background subtraction utilizes the variation in the density of measured events per unit four-dimensional missing-momentum space [2]. This distribution shows a sharp quasilastic peak, and a nearly flat background. The four-dimensional volume element is

$$d\epsilon_m d^3\vec{P}_m \rightarrow d^2\vec{P}_{mT} d\alpha d(m_M^2) \quad (7)$$

where \vec{P}_{mT} is the transverse part of the missing momentum vector as defined in Equation 2, and the longitudinal portion α (α_0) is given by Equations 3 and 4.

Elastic pp scattering occurs at a singular point ($m_M^2 = 0$, $P_{mT}^2 = 0$, $\alpha = 1$) in this four-dimensional phase space. Quasilastic scattering is observed as an enhancement in a region around that elastic singular point in missing momentum space. The basic idea of the extraction of elastic and quasilastic scattering is that the four dimensional peak is distinct from the smooth background and can be identified. In Figure 8 the distribution of events in P_{mT}^2 vs m_M^2 is presented. The only kinematic selection criterion for events displayed in this figure is a selection on light cone momentum for $0.95 < \alpha_0 < 1.05$. From Equation 7 we note that each square bin in Figure 8 represents equal four-dimensional phase space. We assume that the background below the quasilastic scattering peak is smooth. The constant background under the quasilastic peak will be determined from the background level per unit phase space in the region around the peak.

An objective of this analysis is to extract the quasilas-

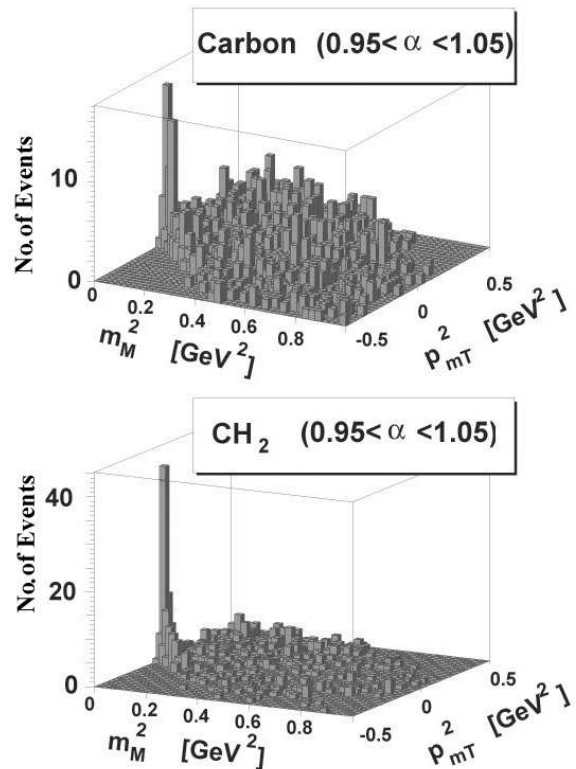


FIG. 8: The distribution of P_{mT}^2 vs m_M^2 for two tracks events observed at beam momentum of 5.9 GeV/c and with $.95 < \alpha_0 < 1.05$. The upper frame shows Carbon data and the lower frame shows CH₂ data. No other kinematic cuts have been applied to these data.

tic signal from background with the inclusion of events that undergo secondary elastic scattering. In the high energy limit, and for quasilastic scattering in the $\alpha = 1$ region, the effect of secondary elastic scattering is to smear the peak seen in Figure 8 to lower m_M^2 and larger P_{mT}^2 . Studies of the data and with Monte Carlo have indicated that we can include nearly all of elastic rescattering in our data sample without accepting excessive levels of background.

With the assumption of smooth background in the $P_{mT}^2 \times m_M^2$ plane, we extract a signal above a constant background using the radial projection of the distribution shown in Figure 8. We define the variable \mathbf{P}^4 to be the sum of the squares of the horizontal and vertical displacement from the elastic peak location,

$$\mathbf{P}^4 \equiv P_{mT}^4 + m_M^4. \quad (8)$$

The distribution of this variable corresponds to a constant four dimensional phase space per $\Delta\mathbf{P}^4$ bin. The distribution of the \mathbf{P}^4 variable has the quasilastic signal concentrating near $\mathbf{P}^4 = 0$ of the distribution as shown for the 5.9 GeV/c data in Figure 9. It is quite natural to extend the smooth background measured in the

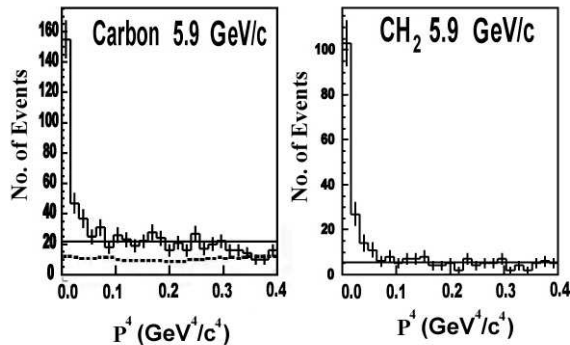


FIG. 9: The distribution of \mathbf{P}^4 variable for the 5.9 GeV/c data set for Carbon and CH_2 targets. The cuts of Equation 9 define these selected events. The dashed line in the Carbon distribution shows the distribution of events, which are explicitly inelastic due to the presence of an extra track in the strawtubes.

interval $0.15 < \mathbf{P}^4 < 0.35(\text{GeV}/c)^4$ in this variable under the quasielastic peak for $\mathbf{P}^4 < 0.1(\text{GeV}/c)^4$. We can test this with events, which are explicitly inelastic by selecting those which have an extra track in the straw tube cylinders. The dashed line plotted in the 5.9 GeV/c Carbon distribution of Figure 9 indicates that the background distribution is indeed flat below the elastic peak.

The distributions of \mathbf{P}^4 are shown in Figure 10 for data collected at 5 beam momenta. The figure shows both distributions for Carbon and CH_2 targets. For data shown in the figure, the event selection is defined by the selection of exactly two nearly back-to-back charged tracks in the spectrometer with a vertex at the appropriate target. Kinematic cuts applied to the events shown in Figure 10 are as follows:

$$\begin{aligned} |P_{mx}| < 0.5\text{GeV}/c, \quad |P_{my}| < 0.3\text{GeV}/c, \\ |1 - \alpha_0| < 0.05, \quad |\theta_3 - \theta_4| < \Delta\theta \end{aligned} \quad (9)$$

The cut, $(|\theta_3 - \theta_4| < \Delta\theta)$, results in a range of c.m. scattering angles in the pp scattering subprocess. The modest differences in angular region are indicated in Table I of the Appendix for each of the 5 beam momentum data sets. This is the same set of cuts used in previously published analysis [1, 2].

The \mathbf{P}^4 distributions for both C and CH_2 are shown for all 5 incident momenta in Figure 10, subject to the cuts of Equation 9. We observe that the level of background relative to signal remains about 10% even as we increase the incident momentum from 5.9 to 14.4 GeV/c. This appears to indicate that the various inelastic background processes decrease with s at least as rapidly as the elastic or quasielastic reactions.

C. THE NUCLEAR TRANSPARENCY RATIO

The secondary interactions associated with quasielastic scattering in this energy range are $\sim 80\%$ absorptive, leading to the break up of one or more of the primary protons. In this analysis elastic secondary scattering introduces minor perturbations in the trajectories of observed final state particles, but it is not expected to reduce the quasielastic event count if the cuts defining quasielastic scattering are fairly open as given by Equation 9. We will compare our observed nuclear transparency to an application of the Glauber model where it is only the absorptive secondary interaction that reduces the nuclear transparency to less than unity. For both the measurement and the Glauber calculation, one must distinguish between the inelastic rescattering which removes the event from the quasielastic channel from a small-angle elastic rescattering which does not. Independent of these difficulties, we observe that the Glauber absorption will be independent of beam energy in this higher energy range. At high energy, elastic rescattering is known to become transverse, exchanging transverse momentum rather than longitudinal momentum with spectator particles. This will smear the transverse components of the reconstructed final state momentum, but will not significantly affect the measured light cone momentum. With this in mind, this analysis will involve selecting data with broad cuts on transverse momentum so that elastic secondary interactions are nearly all included in the event selection in agreement with Monte Carlo simulations

The uncertainties associated with the normalization of the nucleon density distribution is also independent of energy. By relaxing the requirement for an absolute normalization for nuclear transparency, we can make a measurement involving the ratio of cross sections for hydrogen and Carbon. We first calculate the nuclear transparency ratio to establish the energy dependence without reference to specific assumptions about the normalization of the nuclear momentum distribution. In the next section we will use the best nuclear momentum distributions available to compare the absolute normalization of nuclear transparency to the Glauber calculation. so that the two experiments can be directly compared.

The method of analysis for determining the C to H transparency ratio is similar to that discussed previously [1, 28]. Signals for pp elastic and (p,2p) quasielastic events from runs with CH_2 and C targets respectively are extracted from the \mathbf{P}^4 distributions given in Figure 10. Equation 9 lists the kinematic cuts used for the selection. For this set of kinematic cuts, we determined R_C and R_{CH_2} , the event rates per incident beam proton and per Carbon atom in the Carbon or CH_2 targets. Measurements of the thickness of the targets and densities allowed a determination of the Carbon atom densities in the two targets. The yield from the two hydrogen nuclei in the CH_2 target was $R_{\text{CH}_2} - R_C$. Then the experimental nuclear transparency ratio T_{CH} is defined in terms of

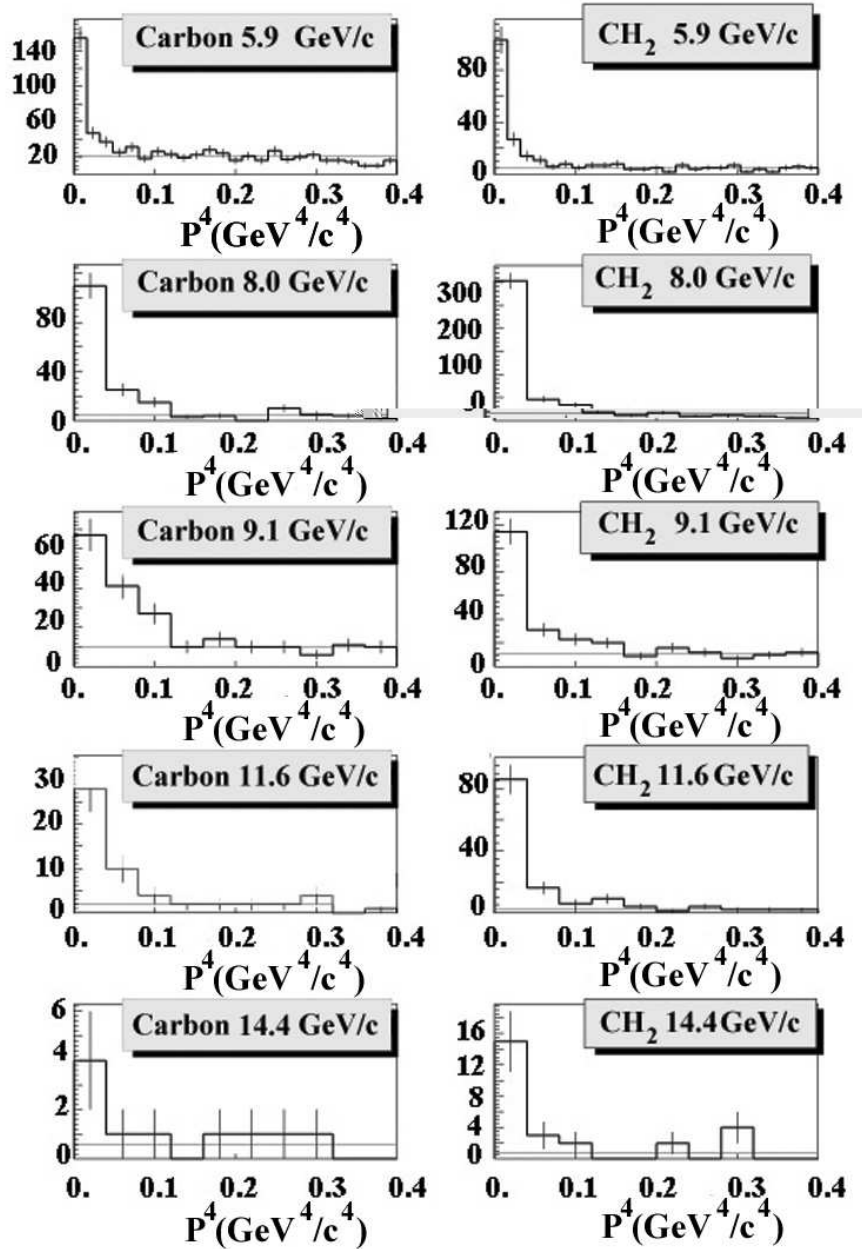


FIG. 10: The \mathbf{P}^4 distribution of events as defined by the cuts of Equation 9 for Carbon and CH_2 targets at each of 5 beam momenta. The horizontal lines show the level of the constant background determined from the $0.15 < \mathbf{P}^4 < 0.35(\text{GeV}/c)^4$ region, and subtracted from under the signal peaks for $\mathbf{P}^4 < 0.1(\text{GeV}/c)^4$.

these event rates,

$$T_{CH} = \frac{1}{3} \frac{R_C}{R_{CH_2} - R_C} \quad (10)$$

The $\frac{1}{3}$ in Equation 10 reflects the relative number of free protons in each CH_2 complex to number of protons in each Carbon nucleus.

There are systematic errors from our fitting and analysis procedures which include: The estimated error in

background subtraction due to variations in the background fitting function of 1%. Target misidentification due to vertex resolution of 2%. Uncertainties in the acceptance calculations of 1%. The maximum beam normalization error is less than 3%. Overall these combined to a 4% error which is small in comparison to the statistical errors.

The values for T_{CH} are plotted in Figure 11a and listed in Table I of the Appendix. We see that there is a strik-

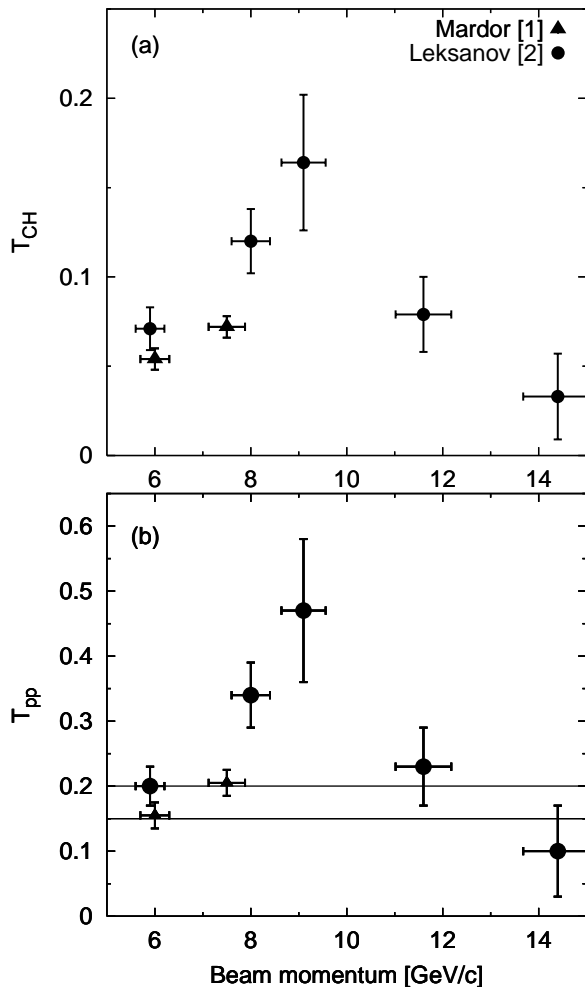


FIG. 11: a.(top frame) The nuclear transparency ratio T_{CH} as a function of beam momentum. b.(bottom frame) The nuclear transparency T_{pp} as a function of the incident beam momentum. The events in these plots are selected using the cuts of Equation 9, and a restriction on the polar angles as described in the text. The errors shown here are statistical errors, which dominate for these measurements.

ing energy dependence in the simple ratio of the rate of Carbon quasielastic events to that of the hydrogen elastic events.

D. THE NUCLEAR MOMENTUM DISTRIBUTION

To determine the nuclear transparencies, T_{pp} , we introduce a relativistic nuclear momentum distribution, $n(\alpha, \vec{P}_{mT})$, that specifies the differential probability density per unit four-momentum. The nuclear momentum distribution is associated with the momentum distribution of protons in the nucleus. We discuss this function as a distribution in light cone momentum, where the differential element is expressed in light cone coordinates.

With Equation 15 below, we can relate the nuclear transparency ratio, T_{CH} , measured over a narrow range of α_1 to α_2 around unity to the nuclear transparency, T_{pp} , over the entire nuclear momentum distribution,

Our formulation of the nuclear momentum distribution parallels the description of a nonrelativistic nucleon momentum distribution by Ciofi degli Atti and Simula [32]. By integrating the spectral function over all removal (missing) energies, E_m , they arrive at their spherically symmetric nucleon momentum distributions, $n(k)$; where k is the wave number. A calculation of the distribution, $n(k)$, requires only a knowledge of the ground-state wave function. In our analysis, we accomplish the same task by using a generous cut in E_m . As discussed in their paper, their nucleon momentum distributions include both the mean field, low momentum component of the distribution, and the high momentum component with NN correlations. The main effect of the NN correlations is to deplete states below the Fermi level, and to make the states above the Fermi level partially occupied as seen in our neutron-proton correlation measurements with the E850 detector [6, 7, 8].

Implicitly integrating over the missing energy, E_m , we characterize the nuclear momentum distribution, $n(\alpha, \vec{P}_{mT})$, over transverse momentum and light cone fraction α . Then we introduce the integral of this nuclear momentum distribution over the transverse coordinates:

$$N(\alpha) = \int \int d\vec{P}_{mT} n(\alpha, \vec{P}_{mT}) \quad (11)$$

The integrated nuclear momentum distributions $N(\alpha)$ can be estimated from nonrelativistic nucleon momentum distributions of Ciofi degli Atti and Simula [32]. Their parameterization for Carbon in terms of the wave number k is:

$$n_C(k) = \frac{1}{4\pi} (2.61e^{-2.66k^2} (1 + 3.54k^2) + .426e^{-1.60k^2} + .0237e^{-.22k^2}) \quad (12)$$

where the units for k and n_C are $Fermi^{-1}$ and $Fermi^{-3}$ respectively. They also provide nucleon momentum distributions for ${}^4\text{He}$, ${}^{16}\text{O}$, ${}^{40}\text{Ca}$, ${}^{56}\text{Fe}$, and ${}^{208}\text{Pb}$ [32].

Equation 12 can be associated with the light cone distribution $N(\alpha)$ by integrating $n_C(k)$ over transverse momentum and by noting that near $\alpha = 1$ as in Equation 3.

$$\alpha \simeq 1 - P_{mz}/m_p. \quad (13)$$

Knowledge of the nuclear momentum distribution represents a practical limit in interpreting the normalization of the nuclear transparency. As we primarily focus on measurements around $\alpha = 1$, it is the normalization of the momentum distribution near the origin that is most critical. The measurement of the shape of the energy dependence of the nuclear transparency can be extracted

with knowledge of the nuclear momentum distribution. However for detailed comparison to the prediction of conventional Glauber absorption, the quantity $N(1)$ must be known. It is fortunate that $N(1)$ is well constrained by a comparison to y scaling data.

It has been pointed out that this dimensionless normalization constant $N(1)$ is connected to $F(y)$, the y scaling function. The y scaling function evaluated at $y=0$ is associated with a transverse integral of the nucleon momentum distribution [33]. The relationship is

$$4\pi \int_0^\infty n_C(p)p^2 dp = 1$$

$$2\pi \int_0^\infty n_C(p)pdp = \frac{1}{m_p}N(1) = F(0) \quad (14)$$

The momentum distribution used here is normalized such that $F(0) = 3.3 \left(\frac{\text{GeV}}{c}\right)^{-1}$, which agrees with y scaling data at about the 10% level.

We can relate the experimentally observed quantity T_{CH} to the a convolution of the fundamental pp cross section with a nuclear momentum distribution $n(\alpha, \vec{p}_{mT})$,

$$T_{CH} = T_{pp} \int_{\alpha_1}^{\alpha_2} d\alpha \int d^2\vec{P}_{mT} n(\alpha, \vec{P}_{mT}) \frac{\frac{d\sigma}{dt}_{pp}(s(\alpha))}{\frac{d\sigma}{dt}_{pp}(s_0)}, \quad (15)$$

where s and s_0 are defined by Equation 5. Further noting that for fixed beam energy the ratio of pp cross sections in Equation 15 is well approximated with a function of α only, we can also write:

$$T_{CH} = T_{pp} \int_{\alpha_1}^{\alpha_2} d\alpha N(\alpha) \frac{\frac{d\sigma}{dt}_{pp}(s(\alpha))}{\frac{d\sigma}{dt}_{pp}(s_0)}. \quad (16)$$

Finally, if the range (α_1, α_2) is restricted to a narrow interval around unity, we see that the relationship between the conventional definition of nuclear transparency T_{pp} and the experimentally measured ratio T_{CH} reduces to a simple proportionality,

$$T_{CH} \simeq T_{pp}N(1)(\alpha_2 - \alpha_1). \quad (17)$$

Our actual determination of the normalization of T_{pp} will be directly obtained from Equation 15 with the evaluation of the integral by the Monte Carlo method, including a weighting of the integrand by experimental acceptance. The shape of the nuclear momentum distribution, taken from work by Reference [32], is used to calculate these integrals. With the normalization fixed, a Monte Carlo program is used to select a region of c.m. angular range where the geometrical acceptance is the same for elastic and quasielastic events. Typically this corresponds to a range of 86° to 90° c.m. as given in Table I of the Appendix.

E. NUCLEAR TRANSPARENCY FOR E850

The evaluation of the integral given in Equation 15 using the form the momentum distribution in Equation 12 yields the nuclear transparency, T_{pp} . Now the measured nuclear transparency can be directly compared to the nuclear transparency calculated in the Glauber Model [12]. The limits of the Glauber prediction are shown as the two horizontal lines in Figure 11b. The limits of the Glauber prediction and uncertainty were calculated using published assumptions [33]. The magnitude of the Glauber nuclear transparency is uncertain at the level indicated but there is a general consensus that Glauber model predicts no significant energy dependence for nuclear transparency in this momentum range. However from the pure pQCD perspective it is unclear what would generate a scale for a peak in the nuclear transparency near 9.5 GeV/c. The probability that the E850 result for the Carbon transparency is consistent with the band of Glauber values is less than 0.3%, and compared to a best fit with a constant transparency of 0.24, the probability is less than 0.8%.

F. Deuteron Transparency

For the earlier experimental run of E850, we used CD_2 as well as CH_2 targets. With an appropriate C subtraction we are able to obtain a D/H ratio as given in Equation 18,

$$T_{DH} = \frac{R_{\text{CD}_2} - R_C}{R_{\text{CH}_2} - R_C}. \quad (18)$$

We include essentially all of the deuteron wave function by using an expanded α_0 interval, $0.85 < \alpha_0 < 1.05$. The T_{DH} transparencies for 5.9 and 7.5 GeV/c incident are 1.06 ± 0.07 and 1.10 ± 0.10 as listed in Table I of the Appendix. The fact that they are consistent with 1.0 provides a further check on the normalization of the nuclear transparency. Further details are to be found in [28].

G. Discussion of angular dependence

Figure 12 shows the angular dependence as well as the momentum dependence for the Carbon transparencies from E850 as reported in Reference [1]. There is a significant decrease in the nuclear transparency at 5.9 GeV/c as $\theta_{c.m.}$ goes from 85° to 90° (probability that the distribution is flat is 0.02%). The poorer statistics at 7.5 GeV/c do not allow any conclusion to be drawn (probability that the distribution is flat is 29%). Measurements of the spin-spin correlation parameter, C_{NN} , show rapid variation of C_{NN} with respect to the c.m. angle near $90^\circ_{c.m.}$. Since these spin-spin correlations are the result of additional scattering amplitudes, they may

also be related to changes in the nuclear transparency. [28, 34, 35].

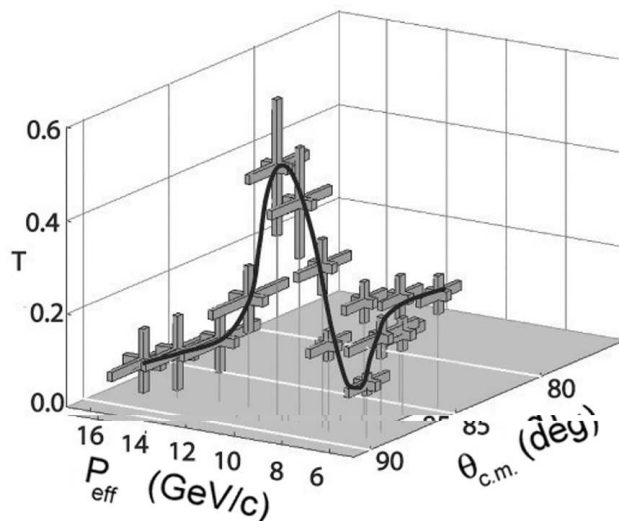


FIG. 12: The dependence of Carbon transparency on effective incident beam momentum (P_{eff}) and on center of mass scattering angle ($\theta_{c.m.}$). The data are from the E850 C(p,2p) experiments.

III. EXPERIMENT E834

This section will describe the nuclear transparency measurements with the E834 detectors during the run of 1987. The analysis methods employed by E834 will be compared to those used in E850.

A. The E834 detector

The E834 detector was originally built for the measurements of a large number of different two body exclusive reactions at $\sim 90^\circ_{c.m.}$ with a liquid hydrogen target [19, 36, 37]. The location of the experiment and the beam line employed was the same as that used later for E850. As indicated in Figure 13, one long-lived, positive particle was detected with a high-resolution magnetic spectrometer with a resolution of ($\Delta p/p = 1\%$). Both the direction and momentum of the particle in the spectrometer were measured with drift chambers DWC 3-4, and DWC 1-2. The acceptance of spectrometer in the scattering plane is $\Delta\theta_{lab} \sim \pm 2^\circ$ and $\sim 5\%$ of the azimuth. An array of very-large-acceptance wire chambers, PWC 3-5, measured the directions of any conjugate particles, which are elastically scattered or resulted from the decay of a resonance. The acceptance of the side chambers was approximately $\pm 30^\circ$ horizontally, and $\pm 35^\circ$ vertically so that nearly all of the quasielastic distribution was measured at one setting. Initial fast triggering was done by the two scintillation hodoscopes, TH1 and TH2, with the assumption

that the interaction occurred within a small axial region of the target. Then a more precise momentum determination for triggering is made with the wires of DWC1 and DWC2. The Čerenkov counters in the spectrometer arm identified pions and kaons so that protons could be selected. Most of the details of the wire chambers, beam and spectrometer Čerenkov counters, and the spectrometer magnet can be found in Reference [19]. When it was realized that measurements of nuclear transparency had an important relationship to exclusive reactions, this apparatus was adapted for that purpose [3].

The liquid hydrogen target was replaced by an array of nuclear targets placed between two planes of lead-scintillator sandwiches to detect possible additional particles in addition to the two protons from a quasielastic scattering. As shown in Figure 14, there were four identical targets of natural isotopic abundances; either Li, C, Al, Cu or Pb. The number of bound protons in the four nuclear targets is approximately 5 times the number of free protons in the two 5 cm long targets of CH_2 on either end. Each of the veto planes consisted of two layers of lead of one radiation length sandwiched between 3, 4.8 mm thick scintillators. Their size was such that 2/3 of the solid angle seen from the target was covered by the veto counters. Events in which charged particles or π^0 's produced signals in two or more layers of scintillator were considered to be inelastic background. The trigger system was set to select events with at least 70% of the momentum of elastic pp events.

The observed distribution of vertices is shown in Figure 15. The four targets of each element were regularly interchanged. The free hydrogen in the two CH_2 blocks provides the normalizer for the nuclear transparency ratio.

B. Kinematics for E834

The kinematic analysis of E834 proceeds along lines similar to that for E850. The equations for missing energy and momentum are similar to those used in E850 (Equations 1).

$$\begin{aligned} \epsilon_m &= E_3 + E_4 - E_1 - m_p \\ \vec{P}_m &= \vec{P}_3 + \vec{P}_4 - \vec{P}_1 \end{aligned} \quad (19)$$

As in E850, the \hat{z} component is along the incident beam direction. The scattering plane, containing the \hat{x} component, is defined as the plane containing \vec{P}_1 and \vec{P}_3 . \vec{P}_3 is the particle traversing the magnetic spectrometer, which has no veto from the spectrometer Čerenkovs. The component of \vec{P}_4 out this plane is a measure of P_{my} .

Since there is a momentum measurement of only \vec{P}_3 , and not \vec{P}_4 , quasielastic reactions are in principle lacking one constraint. However, the missing energy of the struck proton is small compared to the momenta of the initial

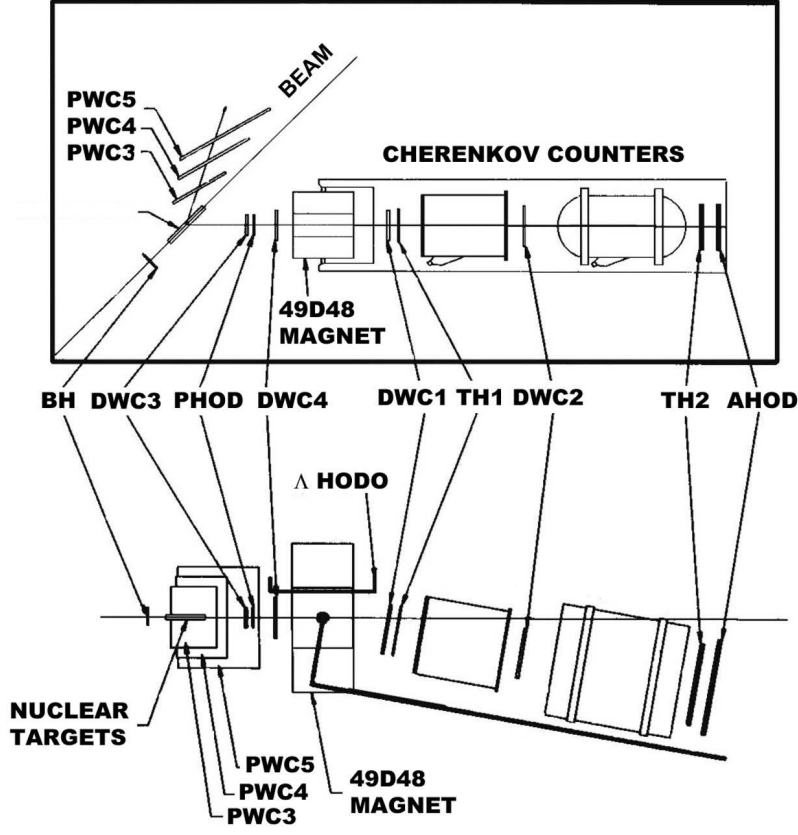


FIG. 13: Schematic drawing of the top and side views of the E834 detector. DWC1 - DWC4 are wire drift chambers and PWC3 - 5 are proportional wire chambers. The two Čerenkov counters detect pions and kaons in the spectrometer, and the scintillation hodoscopes (BH, AHOD and TH1-2) are used for triggering.

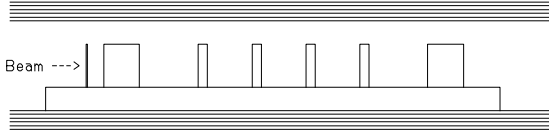


FIG. 14: Schematic side view of target assembly and veto counters for E834 Experiment. Starting from the beam on the left, the elements are the final beam scintillator of 1.5 mm thickness; a 5 cm long CH_2 block, four nuclear targets of either Li, C Al, Cu or Pb; and another 5 cm long CH_2 block. All of these targets rest on a support of light aluminum sheet metal. The length of the top and bottom veto assemblies is 76 cm and their width is 30.5 cm. Each veto assembly consists of 2 layers of lead sandwiched between 3 layers of scintillator

and final state particles. The components of the four momentum \mathbf{P}_m are; $(m_p + \epsilon_m, P_{mx}, P_{my}, P_{mz})$. We neglect ϵ_m , and use energy conservation to solve for E_4 in the first line of Equation 19. Neglecting these terms in the energy balance is a small (0.5%) effect in the determination of the nuclear momenta for quasielastic events [4].

Figure 15b and 15c show how the sharp hydrogen elastic signal is easily extracted from the P_{mz} distributions determined from the lab polar angles of \vec{P}_3 and \vec{P}_4 .

P_{my} is mainly determined by the out-of-plane azimuthal angle, and is only weakly dependent on the magnitude of the momentum of P_3 and P_4 . The difference of the magnitude of the x components of \vec{P}_3 and calculated \vec{P}_4 yield the error on P_{mx} . P_{my} is determined to ± 30 MeV/c, while the error on P_{mx} is deduced to be about ± 100 MeV/c. The transverse components have a negligible effect on center of mass energy s , and since \vec{P}_{my} is the better-determined component, we plot the number of events versus P_{my} as shown in Figure 16a, b and c for Aluminum. The ‘Lego plots’ of missing transverse momentum (P_{mx} versus P_{my}) are shown in Figure 16a and 16b for the Aluminum target data in the quasielastic region. Figure 16a presents all of the events, and Figure 16b shows the distribution after background subtraction. The upper curve in Figure 16c displays the events with no signals from the veto array, and bottom curve displays those events with veto signals in > 1 scintillator planes. The bottom background curve in Figure 16c has

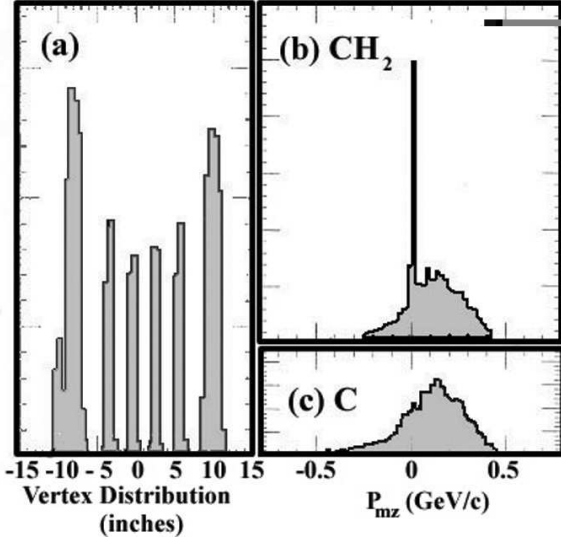


FIG. 15: Vertex distributions of near elastic events for the two CH₂ and four nuclear(Al) targets (a) and p_{mz} distributions from E834 for a CH₂ target (b) and a Carbon target (c). at 5.9 GeV/c.

been multiplied by a constant slightly larger than unity to match the upper curve for the regions $|P_{my}| > 0.50$ GeV/c. The quasielastic signal is the difference of these two curves. The events appearing this plot are selected for $0.9 < \alpha_0 < 1.2$, and have $|P_{mx}| < 0.25$ GeV/c. The events selected as quasielastic are given by the cuts in Equation 20.

$$|P_{mx}| < 0.25\text{GeV}/c, \quad |P_{my}| < 0.25\text{GeV}/c, \quad 0.9 < \alpha_0 < 1.2. \quad (20)$$

The range of $0.9 < \alpha_0 < 1.2$ was selected in the E834 experiment to provide good statistical accuracy from an interval where there is a good signal to background ratio. Also the acceptance of quasielastic and elastic events is nearly identical. Since the CH₂ and nuclear targets were exposed to the same beam, there is automatic beam normalization for the quasielastic and free pp events.

The primary systematic error associated with the E834 experiment is the uncertainty in the background subtraction. The background was determined from the smooth shape fixed by the events with hits in the veto counters, and then normalized to the total distribution for $|P_{my}| > 0.50$. The background to signal is typically 20% with an estimated error $\pm 5\%$.

C. Nuclear Transparencies for E834

Figure 17 shows the comparison of the Carbon transparency measurement of E850 to that reported in our E834 paper. The E834 analysis used a form for the nucleon nuclear momentum distributions, which consisted

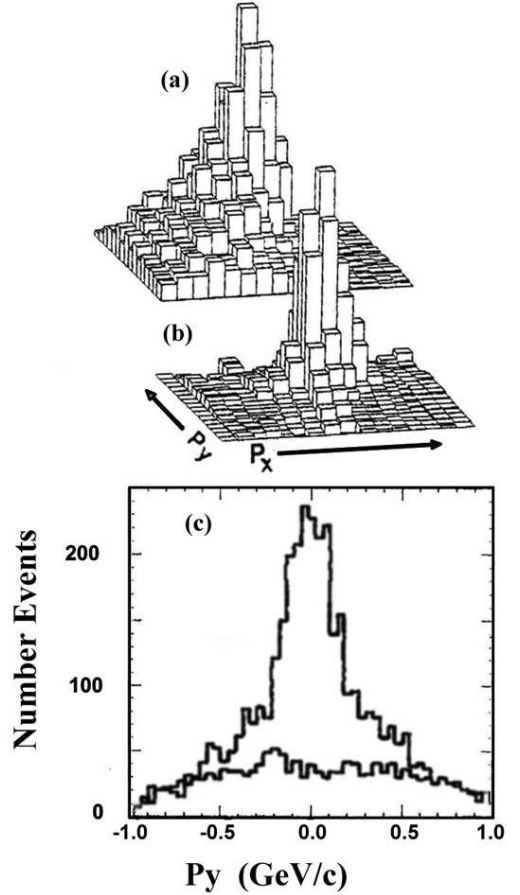


FIG. 16: The distribution of missing transverse momentum (P_{mx} versus P_{my}) at 5.9 GeV/c is shown for aluminum target data in the quasielastic region (a). In (b) the same distribution after background has been subtracted. The projection of (a) for events with $|P_{mx}| < 0.25$ GeV/c and $0.9 < \alpha_0 < 1.2$ is shown in (c). The lower curve represents events with two or more hits in the veto scintillators, and the upper curve is for events without such hits.

of 35% hard sphere with radius of 0.22 GeV/c for Carbon and 65% Gaussian with standard deviation of 0.25 GeV/c fitted to our experimental results [9]. The form of the function, $n_G(p)$, is given below:

$$n_G(p) = \frac{f_f}{[(4/3)\pi p_f^3]} \Theta(p - p_f) + \frac{(1 - f_f)}{[2\pi p_G^2]^{3/2}} \exp\left[-\frac{p^2}{2p_G^2}\right], \quad (21)$$

where f_f is the fraction of the distribution in the Fermi gas distribution; p_f is the radius of the Fermi sphere (0.22 GeV/c for Carbon); and p_G is the radius of the spherical Gaussian (0.25 GeV/c). The step function, $\Theta(p - p_f)$, is 1 inside the Fermi sphere and 0 outside. The relative proportion of hard sphere to Gaussian remains the same, but the radius of the hard sphere is varied from 0.170 to 0.260 GeV/c for Li to Pb nuclei. For this present publication the E834 data are made consistent with the E850 nuclear transparencies by multiplying by the ratio

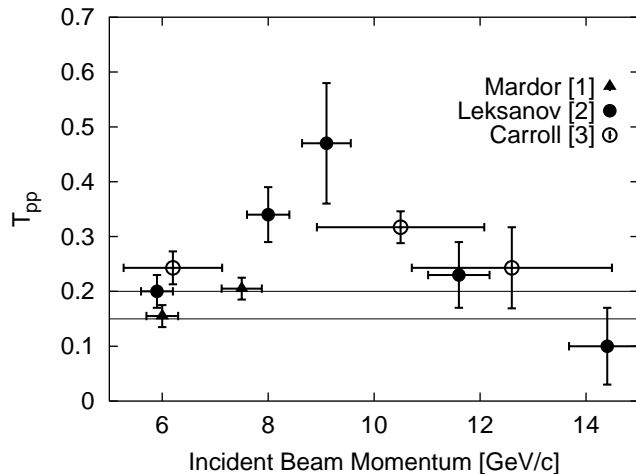


FIG. 17: Comparison of all Carbon transparency (T_{pp}) data from E850 and E834. The 1988 data have been rescaled from published values using the momentum distribution of the form and with the normalization described in reference [32]. The two horizontal lines indicate the range of values for T_{pp} as calculated by the Glauber method [12]. The horizontal error bars represent the total spread in effective momentum resulting from the accepted α_0 range.

of integrated nuclear momentum distributions given in Equation 22.

$$\frac{\int_{pp}}{\int_{E834}} = \frac{\int_{\alpha_1}^{\alpha_2} d\alpha \int d^2\vec{P}_{mT} n_{CS}(\alpha, \vec{P}_{mT}) \frac{d\sigma}{dt}_{pp}(s(\alpha))}{\int_{\alpha_1}^{\alpha_2} d\alpha \int d^2\vec{P}_{mT} n_G(\alpha, \vec{P}_{mT}) \frac{d\sigma}{dt}_{pp}(s(\alpha))} \quad (22)$$

Where n_G is the spherical Gaussian distribution used in E834 as given in Equation 21. n_{CS} are the nuclear momentum distributions derived from Ciofi degli Atti and Simula of the forms given in Equation 12. The E834 transparencies from events in the range of $0.9 < \alpha < 1.2$. listed for Li, C, Al, Cu and Pb are included in Table II of the Appendix.

IV. ENERGY DEPENDENCE OF THE TRANSPARENCIES FROM E834 AND E850

A. Systematic Errors Due to Theoretical Uncertainties

Before we present the theoretical interpretations of our combined results, we will discuss some of the uncertainties connected with the theoretical treatment of elastic scattering from protons bound in nuclei. We have attempted to minimize their effects through our methods of analysis.

As noted earlier, the extraction of nuclear transparency depends on the assumption that the scattering process can be factorized into a product of two functions; the

free pp scattering at an appropriate center of mass energy, s , and a nuclear momentum distribution, $n(\alpha, \vec{P}_{mT})$. This is expected to be a good approximation at high incident momenta and large momentum transfers where the impulse approximation is valid.

In our first 1988 publication we quoted an overall error due to possible off-shell and momentum distribution uncertainties of $\pm 25\%$ [3]. Since then the knowledge of nuclear momentum distributions has been considerably improved. For the combined experiments we have settled on the recent parameterization by Ciofi degli Atti and Simula of the nucleon momentum distributions [32]. Their nucleon momentum distributions are based on a careful study of electron scattering experiments. The nuclear momentum distribution has been measured to large values of the nuclear momentum by studying the enhanced contribution from values of α less than 1.0. We found equivalent distributions in both the transverse and longitudinal directions [5], [38]. The high degree of two-body correlations above the Carbon Fermi level of 220 MeV/c is dramatically verified in our measurement, which correlated neutron momentum with the proton nuclear momentum determined in C(p,2p) reactions with the E850 detector [6], [7].

How to deal with the off-shell nature of the pp scattering in the nucleus is a difficult question. Fortunately, the energies of the experiment are large compared to the nuclear binding energies. However, the s^{-10} energy dependence of the pp cross section magnifies even relatively small effects in the longitudinal direction. The effect of the struck proton being off-shell is liable to suppress the 3-quark Fock state as gluons are exchanged to bring it on-shell. The effect of the binding on the effective s of the interaction, also needs to be considered.

We estimate a systematic error of $\pm 15\%$ for these theoretical uncertainties for this present publication.

B. Combined Nuclear Transparency Data

After unifying the normalization of the E834 and E850 transparencies, we can plot the Carbon transparency results for both experiments as shown in Figure 17. If we interpolate the E850 results to compare to the E834 transparencies at the same incident momentum, then we find very good agreement as to their magnitudes despite the different analysis methods and α ranges. The ratios of $\frac{T_{pp}(E850)}{T_{pp}(E834)}$ at 6.2, 10.5 and 12.6 GeV/c are: 0.91 ± 0.12 , 1.06 ± 0.20 , and 0.76 ± 0.30 .

The most striking aspect of these two experiments is the confirmation of the peak in nuclear transparency at about 9.5 GeV/c incident momentum. Neither the Glauber model nor the naive prediction of the Color Transparency model can explain the data. The range of the conventional Glauber calculation is indicated on the figure by the two horizontal lines at 0.15 and 0.20 [33].

To further emphasize the emerging pattern, we add the aluminum data measured in E834 to all the Carbon results. For consistency, we again must make the correction for differences in nuclear momentum distribution used here and in the E834 analysis. In Table III of the Appendix, the E834 data is corrected first with a ratio of the new to old nuclear momentum distribution integrals. Then from the 1988 analysis of the E834 data it was determined that at fixed energy, the dependence of the nuclear transparency was compatible with the inverse of the nuclear radius, $A^{-1/3}$. So the statistically more precise Aluminum data can be compared to the Carbon transparencies by multiplying by this expected A dependence, $(27/12)^{1/3}$ as shown in Figure 18.

When we include the normalization and shape of the nuclear momentum distribution, we obtain not only transparencies, T_{pp} , at $\alpha = 1$ for the nominal incident momentum, but we can also interpret data for $\alpha \neq 1.0$. We note from Equation 6 that with a fixed incident proton momentum, it is possible to study quasielastic scattering at an extended range of center of mass energies, corresponding to effective beam momentum, P_{eff} , above and below the nominal value.

In Figure 18 we fully exploit our knowledge of the energy dependence of the pp cross section and the nuclear momentum distribution to extract transparencies from the 9, 11.6 and 14.4 GeV runs at larger values of α ($1.05 < \alpha < 1.15$). These points are plotted at their corresponding P_{eff} . We see that they fill in to form

a smooth curve extending to higher energy. In E834, P_{eff} was calculated for 3 bins in α (0.8-0.9, 0.9-1.0, and 1.0-1.2) as given in Table III of the Appendix. These points also fall on a smooth curve between the points corresponding to $\alpha = 1.0$. Figure 18 demonstrates that there is a peak in the nuclear transparency at 9.5 GeV/c nearly independent of whether the combined data set, or the separate E850 and E834 sets are used. Beyond 9.5 GeV/c the nuclear transparency returns to the Glauber level or below at 12 GeV/c and higher momentum.

C. Discussion of Energy Dependence

The initial rise in the nuclear transparency between 5.9 and 9.5 GeV/c was thought to be a manifestation of Color Transparency, namely the expansion of a very small configuration of valence quarks over distances comparable to the nuclear radius. In expansion models, the high P_T interaction is presumed to select nearly point like configurations (plc's) of valence quarks in the interacting protons [11]. These plc's proceed to expand as they recede from the point of interaction. The rate of expansion has been described in both partonic and hadronic representations [39],[40]. Farrar, Liu, Frankfurt, and Strikman suggested a convenient expansion parameterization given by Equation 23 [39]:

$$\sigma_{int}^{eff}(z, Q^2) = \sigma_{int} \left(\left[\left(\frac{z}{l_h} \right)^\tau + \left(\frac{r_t(Q^2)^2}{r_t^2} \right) \left(1 - \left(\frac{z}{l_h} \right)^\tau \right) \right] \theta(l_h - z) + \theta(z - l_h) \right) \quad (23)$$

where σ_{int} is the free pN interaction cross section, l_h is the expansion distance of the protons, and z is the distance from the interaction point. $\sigma_{int}^{eff}(z, Q^2)$ expands linearly or quadratically from its initial size depending on the value of τ , and then assumes the free space value, σ_{int} , when $z = l_h$. The actual value of σ_{int} used in the fitting procedure is less than the free pN total cross section, $\sigma_{tot}(pN) \sim 40mb$, because nearly all ($\sim 90\%$) of the elastic cross section is within the acceptance of our detector. The exponent τ allows for two suggested pictures of expansion. For $\tau = 1$, the expansion corresponds to the quantum diffusion picture [39]. For this picture, $l_h = 2p_f/\Delta(M^2)$ where p_f is the momentum of a proton traveling through the nucleus [39]. At distances comparable to nuclear sizes, the effective cross sections should revert to their free space values. The authors of [39] indicate the values of $\Delta(M^2)$ between 0.5 and 1.1 GeV^2 are acceptable with $\Delta(M^2)=0.7$ being favored. This range of $\Delta(M^2)$ corresponds to values of $l_h = 0.36p_f$ to 0.78 p_f fm. For a momentum of 5.9 GeV/c the expansion dis-

tance will be between 2.1 and 4.7 fm. .

The case of $\tau = 2$ is considered to be the 'naive quark expansion' scenario in which the light quarks fly apart at a maximum rate and the distance is determined by the Lorentz boost to the hadrons. In this case $l_h = \sim E/m_h$ where m_h is the mass of the hadron involved [39]. For protons at 5.9 GeV/c, the expected expansion distance is ~ 7.3 fm. The quantity $\langle r_t(Q^2)^2 \rangle / \langle r_t^2 \rangle$ represents the fraction of σ_{int} at the time of interaction. This quantity is approximated by $\sim 1/Q^2$, corresponding to 0.21 at 5.9 GeV/c and falling with an increase of incident momentum [39].

Since we are dealing with hadrons, Jennings and Miller reasonably suggested that a hadronic representation of the interacting protons should be considered [40]. In this picture, the expansion distance at 5.9 GeV/c should correspond to ~ 0.9 fm for linear expansion, and ~ 2.4 fm for the quadratic case depending on the form of their intermediate state $g(M_x^2)$ [40]. The shape of the expansion is approximated by that given in Equation 23.

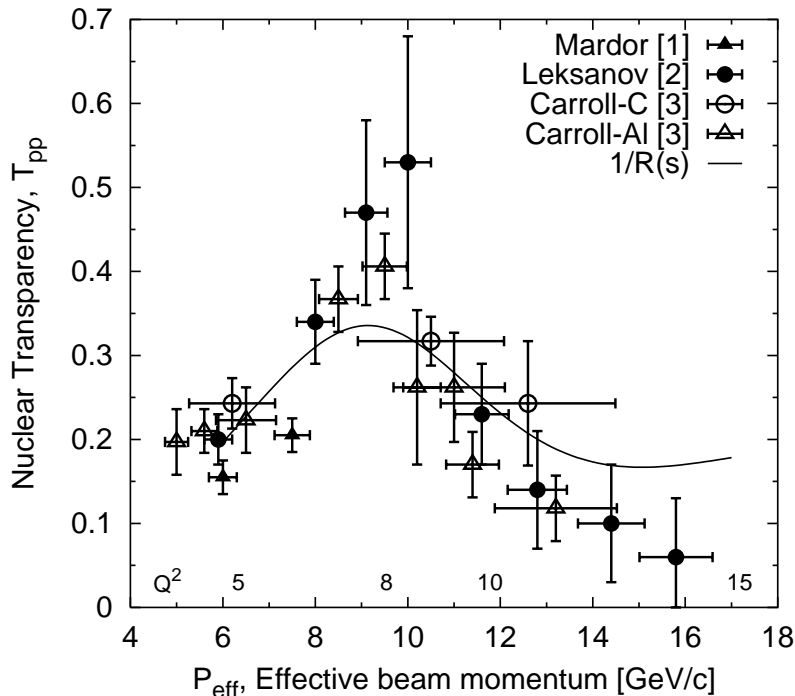


FIG. 18: The T_{pp} values for Carbon and the aluminum (scaled by $(27/12)^{1/3}$) are plotted versus their P_{eff} values. For a single incident beam momentum, P_1 , a range of P_{eff} values is obtained by using Equation 6. This allows us to place more points on the nuclear transparency curve and extend the range of momenta. The curved line is the inverse of $R(s)$ defined by Equation 24, and adjusted with an amplitude for a best fit to the magnitudes of the measured transparencies. The horizontal error bars represent the total spread in effective momentum resulting from the accepted α_0 range. A Q^2 [$(GeV/c)^2$] scale is included at the bottom of the figure.

However, the drop in the nuclear transparency above 9.5 GeV/c requires additional mechanisms. We will discuss two possible explanations that have been introduced for the energy dependence. First, Ralston and Pire [41] suggested that the structure of the nuclear transparency may arise from an interference between two distinct amplitudes that contribute to pp elastic scattering. One amplitude is the hard amplitude that we associate with quarks at small transverse spatial separation for dimensional scaling, which should dominate the high energy cross section. The other amplitude is a soft component, essentially a remnant of the higher order radiative (Sudakov) process that strongly attenuates the large distance part of the proton wave function.

The dependence of the pp elastic cross section near $90_{c.m.}^\circ$ degrees varies nearly as a power of s :

$$\frac{d\sigma}{dt_{pp}}(\theta = 90_{c.m.}^\circ) = R(s)s^{-10}. \quad (24)$$

Compared to the pp cross section, which varies over 5 orders of magnitude, the variation in $R(s)$ is only about a factor of two in the region of s spanned by these experiments [42],[41]. The dependence of the cross section on α will reflect both the nuclear momentum distribution (Equation 12) and the cross section dependence of (Equation 24). The short distance part is predicted to

have an energy dependency that scales as (s^{-10}) . In the picture of Ralston and Pire the long-ranged portion of the amplitude is attenuated by the nuclear matter, and the interference largely disappears for the numerator of Figure 1 but not in the free pp scattering of the denominator [41]. Therefore these authors predicted that this picture would naturally lead to an energy dependence of nuclear transparency, which could vary like $R(s)^{-1}$ where R is defined in Equation 24. The curve $R^{-1}(s)$ is shown on Figure 18 arbitrarily normalized to the approximate scale of the nuclear transparency. This model suggests that the nuclear transparency should rise again at ~ 20 GeV/c.

Another possible perspective on the energy dependence is suggested by Brodsky and deTeramond [43]. They observed that the excess in the pp elastic cross section above the scaled cross section associated with a peak in $R(s)$ at beam momenta above 9.5 GeV/c could correspond to a resonance or threshold for a new scale of physics. They suggested that one candidate involved the charmed quark mass scale corresponding to ~ 12 GeV/c incident protons, but other exotic QCD multi-quark states could also be considered. They connected this resonance model with the anomalous spin dependence of the pp elastic cross section at these energies [34]. In their model, the increase in nuclear transparency from 5.9 to 9.5 GeV/c

is associated with ordinary color transparency but the rapid reduction of nuclear transparency back to Glauber levels would signal a contribution from a new mass scale or new dynamic QCD scale. The connection to the polarization dependence of these cross sections indicates that the new scale behaves like a spin 1 resonance.

We note that our measurement of T_{pp} in the peak region ~ 9.5 GeV/c is approaching 50%, and is more than twice the Glauber level. At the peak, we find that the A(p,2p) Carbon transparency is almost as large as the (e,e'p) nuclear transparency as described in Section VII later. This comparison is surprising and interesting even without reference to a detailed Glauber calculation.

In conclusion, we note that both the Ralston - Pire model and the Brodsky - deTeramond picture can probably accommodate our measurement. The Brodsky - deTeramond model, however, would predict a dramatic dependence of nuclear transparency upon the initial state spins of the protons. We believe that a double spin measurement the nuclear transparency of light polarized nuclei may be the best way to distinguish these two models [44]. A measurement of the A-dependence at 12 GeV/c and above as described in the next section would be valuable. In the Ralston-Pire picture, the absorption cross section would continue to decrease from previous values [41].

V. A DEPENDENCE FROM E834

As well as observing the energy dependence of the Carbon transparency, we also determined the nuclear transparency of Li, Al, Cu, and Pb at incident momenta of 5.9 and 10 GeV/c. Transparencies for Carbon and Aluminum are also determined at 12 GeV/c, but the Carbon transparency has a relatively large error since this transparency was determined from the CH₂ targets rather than a pure Carbon target.. The wide range of radii from Lithium (2.2 fm) to Lead (6.5 fm) enables us to determine the attenuation of protons in nuclear matter, and to determine in an independent manner that the effective absorption cross section is less than that used in Glauber calculations. The numbers of quasielastic events for all the 5 nuclei are extracted in the same manner as for the Aluminum targets in Subsection III B. The cores of the P_{my} distributions are compatible with known electron distributions as seen in Figure 19 [9]. We list in Table II and plot in Figure 20 the transparencies for these 5 nuclei for the range of $0.9 < \alpha < 1.2$. These transparencies have been normalized by multiplying by the ratios of the integrals using Ciofi degli Atti and Simula nucleon momentum distributions to the integrals using the nuclear momentum distributions of the original 1988 analysis as given by Equation 21. For Li, Al and Cu an interpolation between the published nucleon momentum distributions is applied to the integrals. For Li we use ⁴He and ¹⁶O; for Al it is between ¹⁶O and ⁴⁰Ca; and for Cu it is between ⁵⁶Fe and ²⁰⁸Pb [32].

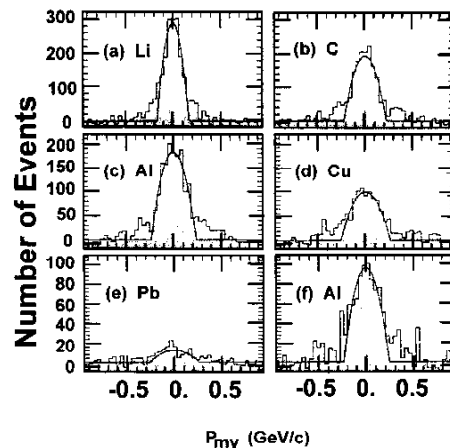


FIG. 19: The missing P_{my} distributions for the 5 elements used in E834 after corrections for acceptance and for background subtraction. Distributions for (a) to (e) are at 5.9 GeV/c, and the distribution (f) is at 10 GeV/c. The form of the model of Moniz, et al is superimposed over each distribution [45].

As can be seen in Figure 20, the 10 GeV/c transparencies of all 5 nuclei are consistently higher than those at 5.9 and 12 GeV/c, in agreement with the energy dependence observed with the Carbon and Aluminum data. The solid lines passing through the 5.9 and 10 GeV/c data points represent fits with a constant effective cross section of $17.9_{-1.5}^{+2.7}$ mb at 5.9 GeV/c and $12.3_{-2.6}^{+2.6}$ for 10 GeV/c, and a floating normalization [46]. These values are consistent with the qualitative analysis performed by Heppelmann [47], and a detailed analysis by Jain and Ralston [48]. Further analysis by Carroll found that most expansion models are not compatible with our measured transparencies [46].

This observation of the energy variation of the attenuation is an independent indication that the absorption of protons for large Q^2 quasielastic events is less than that predicted by free nucleon-nucleon scattering. The errors on the transparencies of the two adjacent nuclei at 12 GeV/c do not allow us to measure the attenuation for this momentum.

VI. (π^+ , π^+p) TRANSPARENCIES

Both E850 and E834 are were performed in secondary hadron beams, and used differential Čerenkov counters

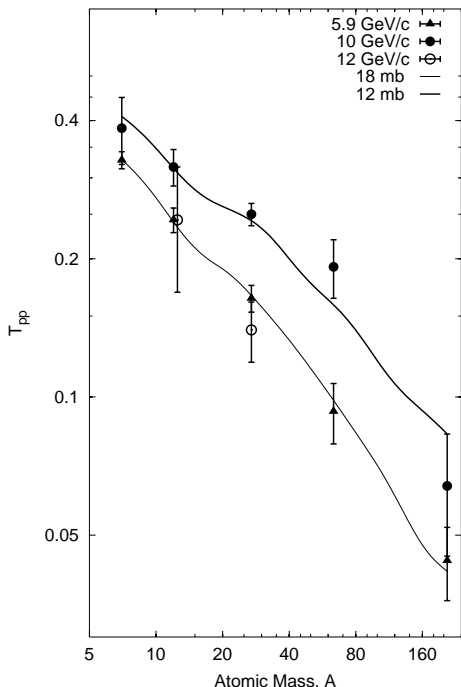


FIG. 20: Nuclear transparency vs Atomic Mass A for the $A(p,2p)$ measurements from E834 for incident momenta of 5.9, 10 and 12 GeV/c as indicated on the figure. The error bars reflect the statistical uncertainties and a 10% target-to-target systematic error. The solid curves represent the fits with constant effective cross sections to the five nuclei at 5.9 and 10 GeV/c as described in the text.

for beam particle identification. The (π^+, π^+p) 90° differential cross sections are 10 to 25 times smaller than the $(p,2p)$ cross sections. However, we were able to make initial measurements of the ratios of the $A(\pi^+, \pi^+p)$ to $A(p,2p)$ transparencies for all 5 targets at 5.9 GeV/c, and for the Al target at 10 GeV/c. We multiply by the $A(p,2p)$ transparencies to obtain the transparencies plotted in Figure 21; these are also tabulated and presented in Table IV of the Appendix [4]. The ratios are measured on the slightly larger interval, $0.8 < \alpha_0 < 1.2$, but the effect is negligible compared to the statistical errors. Due to the large statistical errors, and the measurement of a single transparency at 10 GeV/c, attempts to determine effective cross sections from these $A(\pi^+, \pi^+p)$ transparencies were not useful as they were for the $A(p,2p)$ transparencies in the previous section. We only note that the $A(\pi^+, \pi^+p)$ transparencies are $\sim 1.5\times$ the corresponding $A(p,2p)$ transparencies. More details, including the identification of the π^+ in the beam by the differential counters, can be found in the thesis by J-Y Wu [4].

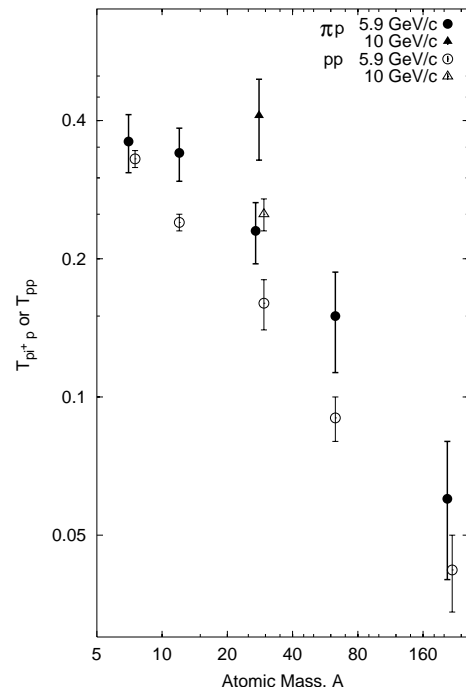


FIG. 21: T_{π^+p} and T_{pp} transparencies for Li, C, Al, Cu and Pb at 5.9 GeV/c, and Al for 10 GeV/c. The T_{π^+p} values (solid symbols) are consistently larger than those of T_{pp} (open symbols).

VII. COMPARISON TO OTHER EXPERIMENTS

The $A(p,2p)$ experiment of Tanihata, *et al.* had 1.46 GeV/c protons incident on a set of 5 different nuclei (ranging from C to Pb in size); their results indicate a mean free path of ~ 2.4 fm [49]. With a nuclear density of $\frac{1}{6} fm^{-3}$, this corresponds to $\sigma = 25mb$. The σ_{tot} for the two outgoing protons of 0.95 GeV/c is $\sim 25mb$ [50]. We therefore conclude that the value of the nuclear transparency, below the minimum momentum studied in our experiments, is close to the Glauber limit.

The other major investigations of nuclear transparency have been with quasielastic scattering in the $A(e,e'p)$ reaction at SLAC [51, 52], and at Jefferson Lab [53, 54]. In these experiments, the nuclear transparency, T_{ep} , as a function of Q^2 is

$$T_{ep}(Q^2) = \frac{\int_V d^3P_m dE_m Y_{exp}(E_m, \vec{P}_m)}{\int_V d^3P_m dE_m Y_{PWIA}(E_m, \vec{P}_m)} \quad (25)$$

where Y_{exp} is the experimental yield of quasielastic scatters, and Y_{PWIA} is the calculated yield in the partial wave impulse approximation. These studies use a prescription for the off-shell σ_{ep} . However, inserting the on-shell form changes $T_{ep}(Q^2)$ by less than 1%.

As seen in Figure 22, these measurements begin with Q^2 below 1 $(GeV/c)^2$, and extend to $Q^2 = 8.1 (GeV/c)^2$.

Above a Q^2 of $\sim 2(\text{GeV}/c)^2$ the measurements are consistent with a constant nuclear transparency for the deuterium, carbon, iron, gold targets. Note that $Q^2 = 8.1 (\text{GeV}/c)^2$ corresponds to an incident proton momentum of 9.5 GeV/c.

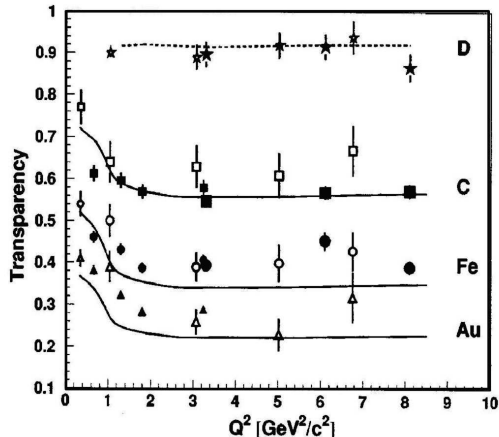


FIG. 22: $(e,e'p)$ transparencies taken from Reference [54]. The open symbols correspond to the SLAC experiments [51, 52], and the closed symbols are from the more recent results of Jefferson Laboratory [53, 54].

The level of nuclear transparency in the nucleus of carbon is predicted by Glauber models to be much larger for $(e,e'p)$ quasielastic scattering, T_{ep} . This is because of the non-absorptive nature of the two legs of the electron diagram as they pass through the nucleus. For example, if T_{ep} for carbon is ~ 0.6 , then one would expect the corresponding T_{pp} to be ~ 0.2 . However, note that the $C(e,e'p)$ nuclear transparency is not much higher than the nuclear transparency for $C(p,2p)$ at its peak. These experiments reported no significant deviation from the Glauber prediction, although the size of the effect would have been smaller than in the $A(p,2p)$ case. This may suggest that the phenomena that we observed may be specific to the QCD dynamics of hard pp collisions. Both the Ralston-Pire and the Brodsky-deTeramond models for energy dependence would apply to pp but not to ep scattering [41, 43]. Both models do, of course, contain elements of color transparency that would be common to ep and pp experiments.

VIII. SUGGESTIONS FOR FUTURE EXPERIMENTS

Clearly there remain a number of interesting investigations involving nuclear transparency of protons and other hadrons. A revival of the AGS fixed target program [44], or the construction of the 50-GeV accelerator as part of the J-PARC complex in Japan [55], would provide excellent opportunities to expand the range of these nuclear

transparency studies. Some of the remaining questions are:

1. What happens at higher incident momentum? Does nuclear transparency rise again above 20 GeV/c, as predicted in the Ralston-Pire picture [56]
2. A dependent studies in the 12 to 15 GeV/c range; will the effective absorption cross section continue to fall after the nuclear transparency stops rising at ~ 9.5 GeV/c? [56]
3. At the higher energy ranges of these experiments the spin effects are expected to be greatly diminished. However, they continue to persist, as shown in both single and double spin measurements [34, 57]. So it is important to see, in quasielastic scattering inside a nucleus, whether a relatively pure pQCD state is selected, and if the spin dependent effects are attenuated
4. Measurements of nuclear transparency with anti-protons, pions and kaons will be informative. These particles have widely different cross sections at $90^\circ_{c.m.}$. For instance, the pp differential cross section at $90^\circ_{c.m.}$ is 50-times larger than the $\bar{p}p$ differential cross section [19]. How should this small size of the $\bar{p}p$ cross section affect the absorption of \bar{p} 's by annihilation?
5. The production of exclusively produced resonances provides a large testing ground for nuclear transparency effects. This is especially true for those resonances that allow the determination of final state spin orientation, such as ρ 's or Λ 's [19, 36]. Will the interference terms that generate asymmetries disappear for reactions which take place in the nucleus?
6. Measurements in light nuclei that determine the probability of a second hard scatter after the first hard interaction are an alternative way to study nuclear transparency effects. With the proper kinematics selected, the probability of the second scatter is dependent on the state of the hadrons at the first hard interaction [58].

IX. SUMMARY

Presented here is a summary of the results and interpretations of our T_{pp} investigation results, as well as other quasielastic experiments.

1. Two separate experimental programs, E834 and E850, that employed entirely different detectors and different analysis methods, showed a consistent and striking energy dependence in the T_{pp} nuclear transparency for effective momenta from 5 to 15.8

GeV/c. This corresponds to a range in Q^2 from 3.9 to 14.0 $(GeV/c)^2$. There is a peak in the nuclear transparency at ~ 9.5 GeV/c. At the peak, the nuclear transparency is a factor of 2 above the maximum expected by the Glauber prediction. For 12 GeV/c and above, the nuclear transparency is at or below the Glauber level. The probability that these transparencies are consistent with a constant is less than 1%. The interpretations for the rise and fall of the A(p,2p) transparencies all involve the presence of two amplitudes in the pp scattering process [41, 43].

2. The A dependent transparencies from E834 provide an independent method for measuring the effective cross section as the incident momentum is raised. At 5.9 GeV/c the cross section is 18 ± 2 mb, while at 10 GeV/c it is 12 ± 2.6 mb.
3. A number of other measurements have been made with the E834 and E850 detectors.
 - a. Measurements on deuterium yielded a nuclear transparency consistent with 1.0, as expected for this small nucleus.
 - b. The angular dependence for T_{pp} at 5.9 GeV/c is unexpectedly sharp.
 - c. An initial measurement for A(π^+ , π^+p) has been made and indicates that the nuclear transparency for π^+p is $\sim 1.5\times$ larger than that for pp.
4. (e,e'p) experiments have shown no energy dependence between $Q^2 > \sim 2(GeV/c)^2$ and $8.1(GeV/c)^2$. Most theoretical interpretations indicate that, unlike the A(e,e'p) case, there are interferences between the long and short ranged (pQCD scaling) amplitudes for A(p,2p) scattering.
5. The same detectors that measured nuclear transparencies can explore many other phenomena. This is especially true for measurements that exploit the abilities of high momentum transfer quasielastic proton scattering to examine the behavior of individual protons in nuclei. These measurements include nucleon-nucleon correlations. Another investigation is the further study of high momentum tails utilizing the enhancement from the s^{-10} behavior of pp scattering.

These two A(p,2p) experiments at the AGS have revealed fascinating phenomena about nuclear transparency and its possible interpretations with QCD. Also E834 and E850 have shown the usefulness of protons as short-ranged probes of nuclear distributions. We hope that future experiments will expand the precision and range of our experiments with protons and other hadrons.

X. ACKNOWLEDGEMENTS

S. Baker, F. J. Barbosa, S. Kaye, M. Kmit, D. Martel, D. Maxam, J. E. Passaneau, and M. Zilca contributed significantly to the design, construction, and testing of the detector components. In particular, F. Barbosa was responsible for the design of straw tube amplifiers and readout system. We are pleased to acknowledge the assistance of the AGS staff in assembling the detector and supporting the experiment. The experiment benefited throughout by the diligent work of our liaison engineers, D. Dayton, J. Mills, and C. Pearson. The continuing support of the department chair, D. Lowenstein, and division head, P. Pile is gratefully acknowledged. This research was supported by the U.S.-Israel Binational Science Foundation, the Israel Science Foundation founded by the Israel Academy of Sciences and Humanities, the U.S. National Science Foundation (Grant No. PHY9501114), and the U.S. Department of Energy (Grant No DEFG0290ER40553)

XI. APPENDIX - NUMERICAL VALUES

In the following appendix the numerical values of the transparencies from E850 and E834 are tabulated in Tables I to IV. The estimated experimental systematic error for each specific experiment is given in each table of transparencies. Also, there is an overall uncertainty of $\pm 15\%$ due to theoretical considerations, as discussed in Subsection IV A, which applies to all the tables.

TABLE I: Table of carbon and deuterium transparencies from E850. Column 1 lists P_1 , the incident beam momentum in GeV/c, and Column 2 gives $\theta_{c.m.}$ gives the range of c.m. angles accepted by the detector. Column 3 lists α_1 and α_2 , the limits to α_0 . α_0 is the approximation to the longitudinal light cone fraction as described in Subsection IIB. P_{eff} is the effective incident momentum resulting from the range of α_0 given by $P_{eff} = 0.5(\alpha_1 + \alpha_2)P_1$. The nuclear transparency ratio of C to H in the interval $\alpha_1 < \alpha_0 < \alpha_2$ is T_{CH} . The value of the integral, $\int_{\alpha_1}^{\alpha_2} \left(\int_{\alpha_1}^{\alpha_2} d\alpha N(\alpha) \frac{d\sigma}{dt_{pp}}(s(\alpha)) \right) \frac{d\sigma}{dt_{pp}}(s_0)$, measures the fraction of the momentum distribution contained with the limits of α and corrects for s dependence of $\frac{d\sigma}{dt_{pp}}$. The inverse of $\int_{\alpha_1}^{\alpha_2}$ multiplies T_{CH} to give the nuclear transparency for A(p,2p) quasielastic scattering, T_{pp} . The experiment specific systematic error is $\pm 4\%$ as discussed in Section IIC. In addition, there is an additional overall uncertainty due to theoretical considerations.

P_1 [GeV/c]	$\theta_{c.m.}$ [Deg]	α_0	P_{eff} [GeV/c]	T_{CH}	$\int_{\alpha_1}^{\alpha_2}$	T_{pp}
E850 Carbon Data: Leksanov, et al (2001), [2]						
5.9	86.2-90	.95-1.05	5.9	0.071 ± 0.012	0.350	0.20 ± 0.03
8.0	87.0-90	.95-1.05	8.0	0.120 ± 0.018	0.350	0.34 ± 0.05
9.1	86.8-90	.95-1.05	9.1	0.164 ± 0.038	0.350	0.47 ± 0.11
11.6	85.8-90	.95-1.05	11.6	0.079 ± 0.021	0.340	0.23 ± 0.06
14.4	86.3-90	.95-1.05	14.4	0.033 ± 0.024	0.340	0.10 ± 0.07
E850 Carbon Data: for $\alpha > 1$, [29]						
9.1	86.8-90	1.05-1.15	10.0	0.059 ± 0.015	0.11	0.53 ± 0.15
11.6	85.8-90	1.05-1.15	12.8	0.016 ± 0.007	0.12	0.14 ± 0.07
14.4	86.3-90	1.05-1.15	15.8	0.007 ± 0.007	0.11	0.06 ± 0.07
E850 Carbon Results: I. Mardor, et al (1998), [1]						
5.9	85.8-90	.95-1.05	5.9	0.054 ± 0.006	0.350	0.16 ± 0.02
7.5	85.8-90	.95-1.05	7.5	0.072 ± 0.006	0.350	0.20 ± 0.02
E850 Deuterium Results: I. Mardor, et al (1988) [1, 28]						
5.9	85.5-90	.85-1.05	5.6	- -	~ 1.0	1.06 ± 0.07
7.5	85.5-90	.85-1.05	7.1	- -	~ 1.0	1.10 ± 0.10

TABLE II: Table of nuclear transparencies for Li, C, Al, Cu, and Pb from E834 [3]. Detector acceptance is $80^\circ < \theta_{c.m.} < 90^\circ$. The average A of this natural isotopic abundance targets is listed. The first three columns have the same meaning as in Table I. The column labeled T_{E834} gives the transparencies as reported in Reference [3]. The ratio of integrals (see Equation 22) listed in Column 5 corrects the approximate nuclear momentum distributions used in E834 with the improved nuclear momentum distributions derived from Reference [32] as employed in the analysis of E850. T_{pp} is the product of T_{E834} with the ratio of these integrals. The experiment specific systematic error is $\pm 5\%$ as discussed in Section IIIB.

P_1 [GeV/c]	α_0	P_{eff} [GeV/c]	T_{E834}	$\frac{\int_{pp}}{\int_{E834}}$	T_{pp}
Lithium(6.9)					
5.9	0.9-1.2	6.2	0.46 ± 0.02	0.713	0.33 ± 0.02
10.0	0.9-1.2	10.5	0.54 ± 0.09	0.713	0.38 ± 0.06
Carbon(12.0)					
5.9	0.9-1.2	6.2	0.33 ± 0.02	0.736	0.24 ± 0.02
10.	0.9-1.2	10.5	0.43 ± 0.04	0.736	0.32 ± 0.03
12	0.9-1.2	12.6	0.33 ± 0.10	0.736	0.24 ± 0.07
Aluminum(27.0)					
5.9	0.9-1.2	6.2	0.23 ± 0.15	0.715	0.16 ± 0.01
10	0.9-1.2	10.5	0.35 ± 0.02	0.715	0.25 ± 0.02
12	0.9-1.2	12.6	0.20 ± 0.03	0.715	0.14 ± 0.02
Copper(63.5)					
5.9	0.9-1.2	6.2	0.13 ± 0.02	0.713	0.09 ± 0.02
10	0.9-1.2	10.5	0.27 ± 0.04	0.713	0.19 ± 0.03
Lead(207.2)					
5.9	0.9-1.2	6.2	0.058 ± 0.010	0.762	0.044 ± 0.008
10	0.9-1.2	10.5	0.084 ± 0.025	0.762	0.064 ± 0.019

TABLE III: Table of Aluminum transparencies from E834 for $\alpha \neq 1.0$. Detector acceptance is $80^\circ < \theta_{c.m.} < 90^\circ$. Columns 1 to 6 have the same meaning as Tables I and II including the correction of the nuclear momentum distributions from those of E834 to E850. Column 7 is the product of $T_{pp}(Al)$ by the approximate A-dependence to compare with the corresponding transparencies for Carbon. The experiment specific systematic error is $\pm 5\%$ as discussed in Section III B.

P_1 [GeV/c]	α_0	P_{eff} [GeV/c]	T_{E834}	$\frac{T_{pp}}{T_{E834}}$	T_{pp}	$T_{pp} \times (\frac{27}{12})^{1/3}$
5.9	.8-.9	5.0	.18 \pm 0.03	.85	0.15 \pm 0.03	0.20 \pm 0.04
5.9	.9-1.0	5.6	.25 \pm 0.03	.65	0.16 \pm 0.02	0.21 \pm 0.03
5.9	1.0-1.2	6.5	.22 \pm 0.04	.78	0.17 \pm 0.03	0.22 \pm 0.04
10	.8-.9	8.5	.32 \pm 0.04	.86	0.28 \pm 0.03	0.37 \pm 0.04
10	.9-1.0	9.5	.48 \pm 0.05	.65	0.31 \pm 0.03	0.41 \pm 0.04
10.	1.0-1.2	11.0	.25 \pm 0.06	.81	0.20 \pm 0.05	0.26 \pm 0.07
12	.8-.9	10.2	.24 \pm 0.08	.85	0.20 \pm 0.07	0.26 \pm 0.09
12	.9-1.0	11.4	.2 \pm 0.04	.66	0.13 \pm 0.03	0.17 \pm 0.04
12.	1.0-1.2	13.2	.12 \pm 0.04	.79	0.09 \pm 0.03	0.12 \pm 0.04

TABLE IV: Table of $A(\pi^+, \pi^+p)$ nuclear transparencies from E834 [4]. The experiment measured T_{π^+p}/T_{pp} ratios, which we have multiplied by the T_{pp} transparencies of Table II to obtain (π^+, π^+p) transparencies. The experiment specific systematic error is $\pm 5\%$ as discussed in Section III B.

P_1 [GeV/c]	α_0	T_{pp}	$\frac{T_{\pi^+p}}{T_{pp}}$	T_{π^+p}
Lithium(6.9)				
5.9	0.8-1.2	0.33 \pm 0.014	1.10 \pm 0.15	0.36 \pm 0.05
Carbon(12)				
5.9	0.8-1.2	0.24 \pm 0.015	1.42 \pm 0.17	0.34 \pm 0.05
Aluminum(27)				
5.9	0.8-1.2	0.16 \pm 0.02	1.39 \pm 0.19	0.23 \pm 0.04
10	0.8-1.2	0.25 \pm 0.02	1.65 \pm 0.31	0.41 \pm 0.08
Copper(63.5)				
5.9	0.8-1.2	0.09 \pm 0.01	1.63 \pm 0.30	0.15 \pm 0.04
Lead(207.2)				
5.9	0.8-1.2	0.044 \pm 0.008	1.45 \pm 0.41	0.06 \pm 0.02

-
- [1] I. Mardor, et al. *Phys. Rev. Lett.* **81**, 5085 (1998).
- [2] A. Leksanov et al. *Phys. Rev. Lett.* **87**, 212301–1 (2001).
- [3] A. S. Carroll et al. *Phys. Rev. Lett.* **61**, 1698 (1988).
- [4] J-Y Wu. *PhD Thesis, Pennsylvania State University*. (1992).
- [5] Y. Mardor et al. *Phys. Lett. B* **437**, 257 (1998).
- [6] J. Aclander et al. *Phys. Lett. B* **453**, 211 (1999).
- [7] A. Tang et al. *Phys. Rev. Lett.* **90**, 042301 (2003).
- [8] A. Malki et al. *Phys. Rev. C* **65**, 015207 (2002).
- [9] S. Heppelmann et al. *Phys. Lett. B* **232**, 167 (1989).
- [10] S. J. Brodsky. *Proceedings of the XIII International Symposium on Multi-particle Dynamics-1982*, edited by W. Kittel, W. Metzger, and A. Stergiou (World Scientific, Singapore, 1982). (1983).
- [11] A. Mueller. *Proceedings of the XVII Rencontre de Moriond*, edited by J. Tran Thanh Van (Editions Frontieres, Gif-sur-Yvette, France, 1982). (1982).
- [12] R. J. Glauber. *Lectures in Theoretical Physics* edited by W. E. Britin et al. (Interscience, New York). (1959).
- [13] L. L. Frankfurt, M. I. Strikman, and M. B. Zhalov. *Phys. Rev. C* **50**, 2189 (1994).
- [14] M. R. Adams et al. *Phys. Rev. Lett.* **74**, 1525 (1995).
- [15] M. Arneodo et al. *Nucl. Phys. B* **429**, 503 (1994).
- [16] K. Ackerstaff et al. *Nucl. Phys. B* **429**, 503 (1994).
- [17] E. M. Aitala et al. *Phys. Rev. Lett.* **86**, 4773 (2001).
- [18] T. F. Kycia. *private communication*.
- [19] C. White et al. *Phys. Rev. D* **49**, 58 (1994).
- [20] D. Andrews et al. *Nucl. Instr. and Meth.* **211**, 474 (1983).
- [21] W. Meng. *Magnetic fields calculated by Opera-3D/Tosca program, Vector Fields Lmted, 24 Bankside, Kidlington, Oxford, OX5 1JE, UK*.
- [22] M. Kmit, M. Montag, A. S. Carroll, F. J. Barbosa, and S. J. Baker. *Large Cylindrical Straw Tube Arrays for the EVA Detector, EP&S Informal Report: 91-4*. (1991).
- [23] J-Y. Wu et al. *Nucl. Instrum. Meth. A* **349**, 183 (1994).
- [24] F. J. Barbosa. *EVA 850 Straw Tube Electronics, E850 Internal Report*. (1991).
- [25] K. K. Raychaudhuri. *PhD Thesis, University of Pennsylvania*. (1977).
- [26] Simon Durrant. *PhD Thesis, Pennsylvania State University*. (1994).
- [27] Yael Mardor. *PhD Thesis, Tel Aviv University*. (1997).
- [28] Israel Mardor. *PhD Thesis, Tel Aviv University*. (1997).
- [29] Aleksey Leksanov. *PhD Thesis, Pennsylvania State University*. (2000).
- [30] Daniel Zhalov. *PhD Thesis, Pennsylvania State University*. (2001).
- [31] F. Karl. *Survey accomplished with ManCat, 3-D theodolite system, Leica Geosystems, Heerbrugg, Switzerland*.
- [32] C Ciofi degli Atti and S. Simula. *Phys. Rev. C* **53**, 1689 (1996).
- [33] L. Frankfurt, M. Strikman, and M. Zhalov. *Phys. Lett. B* **503**, 73 (2001).
- [34] E. A. Crosbie et al. *Phys. Rev. D* **23**, 600 (1981).
- [35] S. J. Brodsky and G. de Teramond. *Phys. Rev. Lett.* **60**, 1924 (1988).
- [36] G. Blazey et al. *Phys. Rev. Lett.* **55**, 1820 (1985).
- [37] B. Baller et al. *Phys. Rev. Lett.* **60**, 1118 (1988).
- [38] I. Yaron, L. Frankfurt, E. Piasetzky, M. Sargsian, and M. Strikman. *Phys. Rev. C* **66**, 024601 (2002).
- [39] G. R. Farrar, H. Liu, L. L. Frankfurt, and M. I. Strikman. *Phys. Rev. Lett.* **61**, 686 (1988).
- [40] B. K. Jennings and G. A. Miller. *Phys. Rev. Lett.* **69**, 3619 (1992).
- [41] John P. Ralston and Bernard Pire. *Phys. Rev. Lett.* **61**, 1823 (1988).
- [42] Archibald W. Hendry. *Phys. Rev. D* **10**, 2300 (1974).
- [43] Stanley J. Brodsky and G. F. de Teramond. *Phys. Rev. Lett.* **60**, 1924 (1988).
- [44] S. Heppelmann. *Proceedings of the AGS-2000 Workshop, edited by L. Littenberg and J. Sandweiss, BNL 52512 Formal Report*. (1996).
- [45] E. J. Moniz et al. *Phys. Rev. Lett.* **26**, 445 (1971).
- [46] A. S. Carroll. *arXiv:hep-ph/0209288*. 2002.
- [47] S. Heppelmann. *Nuc. Phys. B(Proc. Suppl.)* **12**, 159 (1990).
- [48] P.K. Jain and J. P. Ralston. *Phys. Rev. D* **48**, 1104 (1993).
- [49] I. Tanihata, et al. *Phys. Lett. B* **100**, 121 (1981).
- [50] Particle Data Group. *Phys. Rev. D* **66**, 010001–261 (2002).
- [51] N.C.R. Makins et al. *Phys. Rev. Lett.* **72**, 1986 (1994).
- [52] T.G. O'Neill et al. *Phys. Lett. B* **351**, 87 (1995).
- [53] D. Abbott et al. *Phys. Rev. Lett.* **80**, 5072 (1998).
- [54] K. Garrow et al. *Phys. Rev. C* **66**, 044613 (2002).
- [55] Y. Yamazaki et al. *Joint Project of KEK/JHF and JAERI/NSP, in Proc. of 1999 Part. Accelerator Conf.* (2000).
- [56] Pankaj Jain, Bernard Pire, and John P. Ralston. *Phys. Rept.* **271**, 67 (1996).
- [57] S. Saroff et al. *Phys. Rev. Lett.* **64**, 995 (1990).
- [58] L. L. Frankfurt, W. R. Greenberg, G. A. Miller, M. M. Sargsian, and M. I. Strikman. *Phys. Lett. B* **369**, 201 (1996).